Monthly Notices
of the
ROYAL ASTRONOMICAL SOCIETY

MNRAS **434,** 2069–2093 (2013)
Advance Access publication 2013 July 17

doi:10.1093/mnras/stt1153

HALOGAS observations of NGC 5023 and UGC 2082: modelling of non-cylindrically symmetric gas distributions in edge-on galaxies

P. Kamphuis,[1,2]★† R. J. Rand,[3] G. I. G. Józsa,[4,5] L. K. Zschaechner,[3] G. H. Heald,[4] M. T. Patterson,[6]‡ G. Gentile,[7,8] R. A. M. Walterbos,[6] P. Serra[4] and W. J. G. de Blok[4,9]

[1]*CSIRO Astronomy & Space Science, PO Box 76, Epping, NSW 1710, Australia*
[2]*Astronomisches Institut Ruhr-Universität Bochum, Universitätstrasse 150, D-44801 Bochum, Germany*
[3]*Department of Physics and Astronomy, University of New Mexico, 1919 Lomas Blvd NE, Albuquerque, NM 87131-1156, USA*
[4]*ASTRON, the Netherlands Institute for Radio Astronomy, Postbus 2, NL-7990 AA Dwingeloo, the Netherlands*
[5]*Argelander-Institut für Astronomie, Auf dem Hügel 71, D-53121 Bonn, Germany*
[6]*Department of Astronomy, New Mexico State University, PO Box 30001, MSC 4500, Las Cruces, NM 88003, USA*
[7]*Sterrenkundig Observatorium, Ghent University, Krijgslaan 281 S9, B-9000 Ghent, Belgium*
[8]*Department of Physics and Astrophysics, Vrije Universiteit Brussel, Pleinlaan 2, B-1050 Brussels, Belgium*
[9]*Astrophysics, Cosmology and Gravity Centre, Department of Astronomy, University of Cape Town, Private Bag X3, Rondebosch 7701, South Africa*

Accepted 2013 June 21. Received 2013 June 20; in original form 2013 April 8

ABSTRACT

In recent years, it has become clear that the vertical structure of disc galaxies is a key ingredient for understanding galaxy evolution. In particular, the presence and structure of extra-planar gas has been a focus of research. The Hydrogen Accretion in LOcal GAlaxieS (HALOGAS) survey aims to provide a census on the rate of cold neutral gas accretion in nearby galaxies as well as a statistically significant set of galaxies that can be investigated for their extra-planar gas properties. In order to better understand the vertical structure of the neutral hydrogen in the two edge-on HALOGAS galaxies NGC 5023 and UGC 2082, we construct detailed tilted ring models. The addition of distortions resembling arcs or spiral arms significantly improves the fit of the models to these galaxies. In the case of UGC 2082, no vertical gradient in rotational velocity is required in either symmetric models nor non-symmetric models to match the observations. The best-fitting model features two arcs of large vertical extent that may be due to accretion. In the case of NGC 5023, a vertical gradient is required in symmetric models ($\mathrm{d}V/\mathrm{d}z = -14.9 \pm 3.8\,\mathrm{km\,s^{-1}\,kpc^{-1}}$) and its magnitude is significantly lowered when non-symmetric models are considered ($\mathrm{d}V/\mathrm{d}z = -9.4 \pm 3.8\,\mathrm{km\,s^{-1}\,kpc^{-1}}$). Additionally, it is shown that the underlying disc of NGC 5023 can be made symmetric, in all parameters except the warp, in non-symmetric models. In comparison to the 'classical' modelling, these models fit the data significantly better with a limited addition of free parameters.

Key words: galaxies: haloes – galaxies: individual: NGC 5023 – galaxies: individual: UGC 2082 – galaxies: ISM – galaxies: kinematics and dynamics – galaxies: structure.

1 INTRODUCTION

In the last decade, it has become clear that extra-planar gas is common in spiral galaxies (Rossa & Dettmar 2003; Sancisi et al. 2008). Understanding the physics that govern this extra-planar gas as well as the disc–halo connection in these galaxies has become an important part of understanding how galaxies evolve. Currently, the average cold neutral gas accretion rate is estimated at $0.2\,\mathrm{M_\odot\ yr^{-1}}$ for spiral galaxies (Sancisi et al. 2008). It is difficult to relate this to the amount of gas that is converted into stars because the current star formation rate (SFR) in spiral galaxies varies throughout their discs as well as from galaxy to galaxy. However, considering the median SFR of $3\,\mathrm{M_\odot\ yr^{-1}}$ in the local Universe (Bothwell et al. 2011) most galaxies would consume all their gas in ∼1 Gyr were it not replenished, possibly through the accretion of hot or cold gas (Kereš et al. 2005), or the consumption time extended through recycling (Kennicutt, Tamblyn & Congdon 1994). The halo of a galaxy will form its connection with the intergalactic medium (IGM) and is the location where gas that is brought up from the disc

★ E-mail: peter.kamphuis@csiro.au
† Humboldt Fellow.
‡ Visiting Astronomer, Kitt Peak National Observatory, National Optical Astronomy Observatory, which is operated by the Association of Universities for Research in Astronomy (AURA) under cooperative agreement with the National Science Foundation.

through galactic fountains (Shapiro & Field 1976; Bregman 1980) or chimneys (Norman & Ikeuchi 1989) resides. Therefore, it is clear that it plays a significant role in galaxy evolution.

In this paper, we will adopt the following definitions when discussing the distribution of hydrogen gas in galaxies. As standard practice, we define z as the distance from the galaxy mid-plane and refer to the H I density profile along the z-axis as the vertical profile. We define the main H I disc as the gas component with the narrowest vertical profile which can be described by a function of z/z_0, where z_0 is the characteristic scaleheight. All gas in excess of this main disc will be referred to as extra-planar gas (or halo gas). Several different extra-planar gas components have been identified in the literature and we refer to them in the following manner. Whenever the smooth vertical gas distribution requires a second characteristic scaleheight to adequately describe the data, and this gas is rotating coherently with the main disc, this second component will be called a thick disc.[1] We would like to stress here that this definition does not imply or require hydrostatic equilibrium of this thick disc. Distinct elongated structures outside the main disc will be referred to as filaments or streams. These could originate from the disc as well as from outside the galaxy. Finally, there are extra-planar clouds, e.g. the high- and intermediate-velocity clouds in our own Milky Way (Muller, Oort & Raimond 1963; Wakker & van Woerden 1997) or the counter-rotating clouds in NGC 891 (Oosterloo, Fraternali & Sancisi 2007).

The number of spiral galaxies which are observed to the required sensitivity for detecting extra-planar gas, in H I as well as other wavelengths, has steadily grown over the past few years (Swaters, Sancisi & van der Hulst 1997; Schaap, Sancisi & Swaters 2000; Lee et al. 2001; Fraternali et al. 2002; Barbieri et al. 2005; Westmeier, Braun & Thilker 2005; Boomsma et al. 2008; Zschaechner et al. 2011). First and foremost, there is the very thick H I disc around NGC 891 (Swaters et al. 1997; Oosterloo et al. 2007). This disc contains about 30 per cent of the total H I mass of this galaxy and shows up as a distinct component in the vertical profile of the gas (Oosterloo et al. 2007). Possibly one of the most notable features in the neutral gas of NGC 891 is the decline of its rotational velocities as a function of vertical distance to the plane (Fraternali et al. 2005), the so-called 'lag'. This lag is determined to be linear with a magnitude of $\sim -16\,\mathrm{km\,s^{-1}\,kpc^{-1}}$ in the vertical direction and confirmed in the ionized gas (Heald et al. 2006; Kamphuis et al. 2007a).

This lag has become an important observational diagnostic for understanding the physics of the disc–halo interface. Simulations have shown that the inferred lags cannot be explained by purely ballistic models of galactic fountains alone (Collins, Benjamin & Rand 2002; Heald et al. 2007; Fraternali & Binney 2008) – these underpredict the observed lags. There are several theoretical possibilities that could remedy this discrepancy. First, if the clouds that are expelled from the disc interact with an existing hot halo that has sufficiently slow rotation, it may absorb the angular momentum of the clouds and thus explain the observed steep vertical rotational velocity gradients (Marinacci et al. 2011). Even more so, the cold gaseous clouds travelling through the hot halo could be crucial in cooling the hot halo gas, thus replenishing the gas supply in the disc. Alternatively, the accreted cold gas might flow down on to the disc along the angular momentum axis in a cylindrical fashion naturally causing the observed vertical rotational velocity gradients (Kaufmann et al. 2006). And lastly, it has been shown that, under the right conditions, the gradients could even exist in static distributions (Benjamin 2002; Barnabè et al. 2006) while in fountain models, the effects of radial pressure gradients and magnetic tension could affect lags.

Observations indicate that the extra-planar gas is a combination of accreted gas and gas originating from the disc. The low metallicity of several high velocity clouds (HVCs) surrounding the Milky Way (van Woerden & Wakker 2004) and the presence of filaments and other irregular extra-planar gaseous structures in nearby galaxies (Sancisi et al. 2008) imply that the extra-planar gas must partially come from gas that has been accreted from the IGM and/or companion galaxies. On the other hand, the fact that in some nearby galaxies the extra-planar H I is concentrated towards the disc (Oosterloo et al. 2007) or that the majority of high velocity gas is located near the star-forming inner disc (Boomsma et al. 2005) implies that a large part of this gas originates in the disc. However, the relative contributions as well as the underlying physics remain ill-understood.

A lag has now been observed in several galaxies besides NGC 891 (Heald et al. 2007; Zschaechner et al. 2012). However, the number of galaxies where this lag is actually quantified remains limited (see Zschaechner et al. 2012, for a recent overview). As the vertical gradients are mostly quantified in edge-on galaxies, their determinations are subject to severe line-of-sight effects (Sancisi & Allen 1979). One of the major uncertainties in the research up to now is that non-cylindrically symmetric distributions in or above the plane, besides any possible warping or flaring of the disc, have not been considered. This is a serious concern as it is well known that star formation (SF) predominantly takes place in the spiral arms. Therefore, if the extra-planar gas is pushed out of the plane through galactic chimneys created by the massive stars, it is natural to expect that the extra-planar gas is also preferentially located above the arms. There are indications that such an effect takes place in the ionized gas of NGC 891 (Kamphuis et al. 2007b).

Because the dynamics of the extra-planar gas are to a large degree governed by gravity an interesting subset of galaxies to consider are smaller galaxies. There is observational evidence that in smaller galaxies ($v_{\mathrm{rot}} \leq 120\,\mathrm{km\,s^{-1}}$) the potential becomes too weak to collapse the dust component into a well-defined thin disc (Dalcanton, Yoachim & Bernstein 2004), i.e. thinner than the stellar disc. This indicates that the complex interplay between gravity and other physics governing the evolution of galaxies undergoes a significant change at galaxies of this characteristic size. Results from H I studies in such small galaxies have varied significantly. Matthews & Wood (2003) found tentative evidence for a significant lagging thick disc in UGC 7321 whereas NGC 4244 displays a lag without a clear extra-planar component (Zschaechner et al. 2011). And in UGC 1281, no extra-planar gas nor lag are required (Kamphuis et al. 2011), albeit in this last case a lag cannot be completely excluded. These results clearly show that more detailed investigations into the H I distribution in lower mass galaxies are required before they can be treated as a significant subsample of galaxies.

With the continued development of the Tilted Ring Fitting Code (TIRIFIC) (Józsa et al. 2007) asymmetric distributions[2] and their effects on the apparent vertical gradient can now be explored. We will do this here through comparison with deep H I observations of the small edge-on galaxies NGC 5023 and UGC 2082. These

[1] Note that previously this component has also been referred to as an H I gaseous halo. We prefer not to use this term to avoid confusion with the common understanding of haloes as roughly spherical mass distributions.

[2] A full description of the current version of TIRIFIC, as well as the latest release, can be found at http://www.astron.nl/∼jozsa/tirific/.

Table 1. Basic parameters of the galaxies.

Parameter	NGC 5023	UGC 2082	Ref.
Morphological type	Scd	Scd	2
Centre (α J2000)	$13^h12^m11\overset{s}{.}83$	$2^h36^m16\overset{s}{.}6$	1
(δ J2000)	44° 2′ 16.″9	25°25′20″	1
v_{sys} (km s^{-1})	405	705	1
Distance (Mpc)	6.6	14.4	3
M_B (mag)	–17.29	–18.55	3
D_{25} (arcmin)	6.8	5.8	3
D_{25} (kpc)	13.1	24.3	3
$D_{H\,I}$ (arcmin)[a]	9.7	10.5	1
$D_{H\,I}$ (kpc)[a]	18.6	43.8	1
Total H I Mass ($M_\odot$)	6.1×10^8	2.54×10^9	1
v_{max} (km s^{-1})	89	98	1
SFR ($M_\odot$ yr^{-1})	0.039	0.041	4

Notes. References are: (1) This work, (2) de Vaucouleurs et al. (1992), (3) Heald et al. (2011) and references therein, (4) Heald et al. (2012).
[a]The diameter of the galaxy at a column density of 10^{20} cm^{-2}.

observations were done as part of the Westerbork Hydrogen Accretion in LOcal GAlaxieS (HALOGAS) survey (Heald et al. 2011) on the Westerbork Synthesis Radio Telescope (WSRT). HALOGAS has observed 22 spiral galaxies to sufficient depth (typical column densities of ∼a few times 10^{18} cm^{-2} at typical linewidths in normal spiral galaxies) to detect extra-planar gas, of which a significant subsample (12 galaxies) is of lower dynamical mass. It provides some of the deepest line-emission observations ever performed on spiral galaxies and aims to provide a consensus on the current cold gas accretion rate as well as detect any correlation between the SFR and extra-planar gas in nearby galaxies.

Even though, at their assumed distances, UGC 2082 is more than twice the physical size of NGC 5023 (see Table 1 for their basic parameters), both have a fairly low, but non-negligible, SFR. However, due to their low potential this could still lead to an extra-planar component when gas is ejected through SF processes. Although small galaxies are not expected to accrete baryonic matter at lower redshifts (Hoeft & Gottlöber 2010), both NGC 5023 and UGC 2082 are in the transition region between accreting and non-accreting galaxies, and therefore a modest amount of lagging extra-planar gas might be present if the vertical gradient is predominantly formed by the accretion of matter.

This paper is structured as follows. In Section 2, we will describe the data reduction and observations. Section 3 will contain the models for NGC 5023 and Section 4 for UGC 2082. We will discuss our results in Section 5 and provide a summary in Section 6.

2 OBSERVATIONS AND DATA REDUCTION

2.1 21 cm line observations

The 21 cm line, or H I, observations were obtained with the WSRT as a part of the HALOGAS programme (Heald et al. 2011). After the standard HALOGAS reduction and calibration (Heald et al. 2011) additional analysis was performed with the GIPSY package (van der Hulst et al. 1992). The final cube of NGC 5023 (UGC 2082) was reduced to 69 (72) velocity channels and was offline Hanning smoothed which resulted in velocity resolution of 4.12 km s^{-1}. For the analysis of the neutral hydrogen, two cubes with different spatial resolution were used. One cube at a high resolution of FWHM = 19 arcsec × 13 arcsec (FWHM = 29 arcsec × 13 arcsec) and one at a lower resolution and almost circular beam of FWHM = 36 arcsec × 33 arcsec (FWHM = 41 arcsec × 33 arcsec). This results in physical resolutions of 0.6 × 0.4 kpc (2.0 × 0.9 kpc) and 1.2 × 1.1 kpc (2.9 × 2.3 kpc) for the high- and low-resolution cubes, at given distance. In this paper, only the high-resolution cube is displayed, unless noted otherwise. However, results presented here are always checked for inconsistencies against the lower resolution cubes.

2.2 Individual features

Even though this paper deals primarily with modelling the global structures of NGC 5023 and UGC 2082, we would like to point out several individual features that are visible in the data. The reason for this is twofold. First, cataloguing these features, some of which are potential tracers of cold gas accretion, helps to obtain a clear picture of the cold gas accretion in the local Universe. The second reason is that these features are localized deviations on top of the smooth underlying disc. Therefore, it is important to ignore these features when trying to fit global models to the data. In order to do this consistently, the individual features need to be identified.

2.2.1 NGC 5023

NGC 5023 shows three large distinct H I features. These features are clearly visible in the low-resolution zeroth-moment map shown in Fig. 1, as pointed out by the arrows. This map is made with the assumption of a negligible optical depth in the H I observations. The underlying grey-scale shows a 30 min Hα exposure from the Mosaic 1.1 Imager on the 4 m Mayall Telescope at Kitt Peak National Observatory (Patterson et al., in preparation). Two of the features are located on the south-east side (negative vertical offset) of the disc on opposite sides of the centre. One is seen over the radial range +25 arcsec to +100 arcsec (south-east) at vertical offsets of ∼−75 arcsec (Fig. 1, Arrow 1) and the other further from the centre at radial offsets of −150 arcsec to −50 arcsec (Fig. 1, Arrow 2) but at a similar vertical offset. The third feature can be seen on the north-west side of the galaxy opposite to the second feature at positive vertical offsets (Fig. 1, Arrow 3). All three features are coherent structures in velocity space spanning a range of roughly 60 km s^{-1}. These parameters are summarized in Table 2. Unfortunately, we were unable to obtain individual masses for these features as they are too integrated with the disc. We will return to the possible origin of these features in the discussion, but will initially ignore them in the modelling.

It is interesting to note that the features do not seem to extend beyond the edge of the Hα disc (although feature 3 is right at the edge), which may imply a connection with the underlying SF. Rand (1996) detected an extra-planar ionized hydrogen region in the quadrant of feature 2; however, this ionized gas is offset (in projection) by 1.5 arcmin (2.9 kpc) from this feature. The two brightest Hα regions in the southern part of the disc, underlying feature 1, show diffuse extensions in the image presented here. The extension around the most southern region is notable because it resembles an hourglass shape. These correlations with the Hα emission are interesting to note but mean little by itself. A multiwavelength analysis would be necessary to understand the correlation with the SF in the disc. As such an analysis is beyond the scope of this paper, we refer the reader to a future paper where this analysis will be done to the full extent.

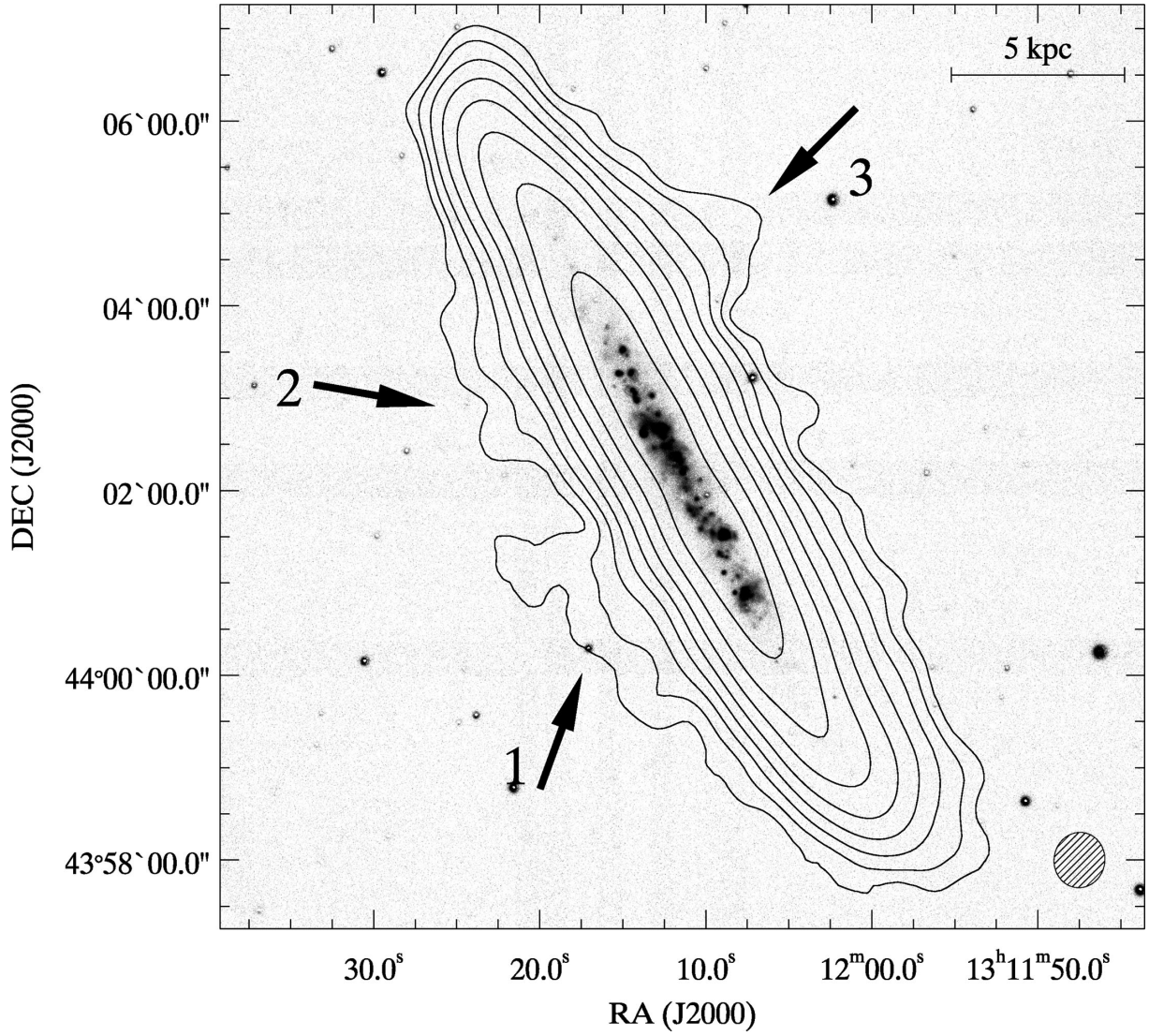

Figure 1. NGC 5023: contours of the low-resolution H I overlaid on an Hα image (see the text) of NGC 5023. The contour levels are $2^n \times 10^{19}$ cm^{-2}, $n = 1-8$. The arrows point out the features discussed in the text and the beam is shown in the lower-right corner (36 arcsec × 33 arcsec) $3\sigma = 8.3 \times 10^{18}$ cm^{-2} for a width of 16.48 km s^{-1} (four channels).

Table 2. Features found in the low-resolution cube for NGC 5023 and UGC 2082. V_0 is the central velocity and $\Delta V_{\rm FWZI}$ the full width at zero-intensity of the specific feature.

Feature	Major axis distance (arcsec)	Minor axis distance (arcsec)	Mass (10^5 M$_\odot$)	V_0 (km s^{-1})	$\Delta V_{\rm FWZI}$ (km s^{-1})
		NGC 5023			
1	72	−80		380	56
2	−112	−92		444	40
3	−120	76		444	52
		(1 kpc = 31.25 arcsec)			
		UGC 2082			
1	156	112	5.8	638	25
2	28	160	13	712	58
3	−16	112	9.6	700	24
4	−72	116	9.8	729	20
5	−140	92	10	758	28
		(1 kpc = 14.3 arcsec)			

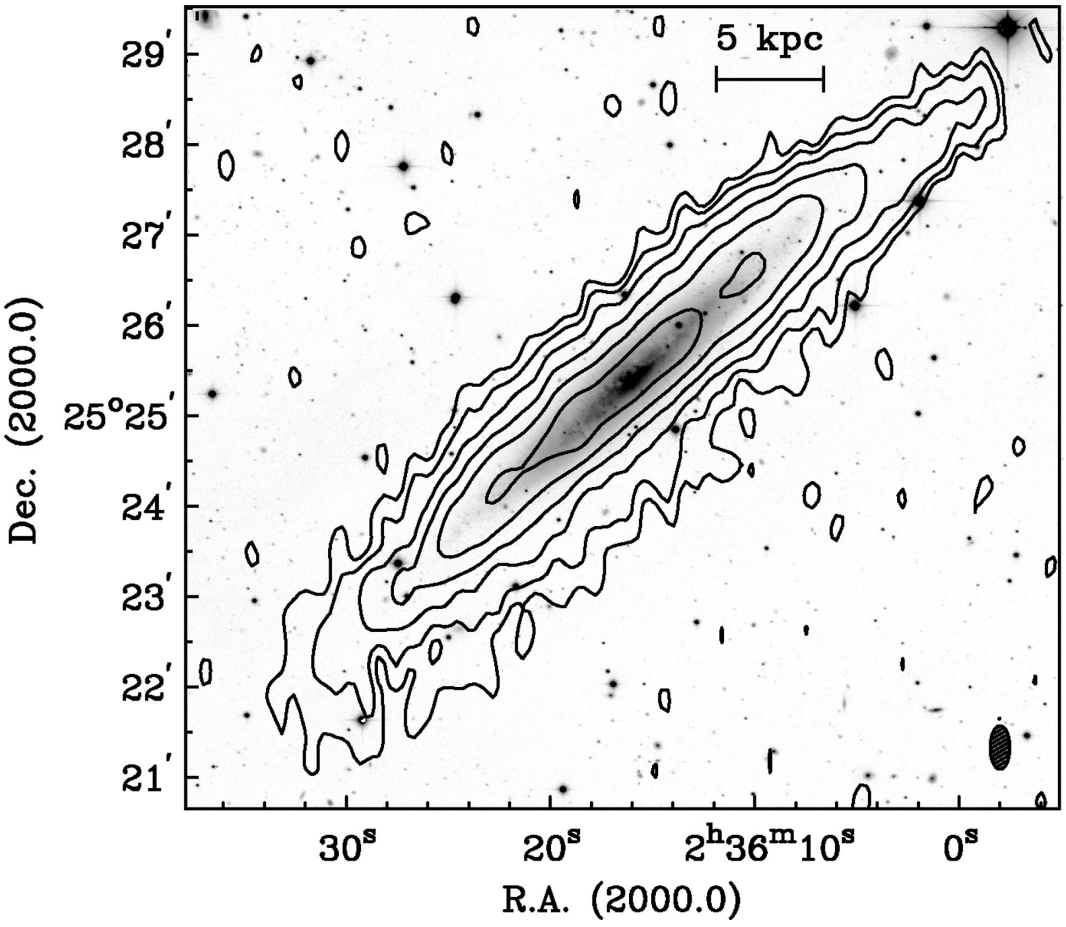

Figure 2. UGC 2082: contours of H I overlaid on an r'-band image (see the text) of UGC 2082. The contour levels are $2^n \times 5.1 \times 10^{19}$ cm^{-2}, $n = 1-6$. The beam is shown in the lower-right corner (29 arcsec × 13 arcsec). $3\sigma = 4.3 \times 10^{19}$ cm^{-2} for a width of 16.48 km s^{-1} (four channels).

2.2.2 UGC 2082

Fig. 2 shows H I contours from our full-resolution map overlaid on an r'-band image taken with the Isaac Newton Telescope as part of the HALOSTARS project associated with HALOGAS. The exposure time of the image is 2398 s (see Gentile et al. 2013 for additional details). UGC 2082 was not detected in the deep Hα survey of Rossa & Dettmar (2003). Five features, all above the N side of the disc, were found in the low-resolution cube with 4σ peaks in at least two consecutive channels. Their parameters are listed in Table 2. None is counter-rotating with respect to the disc emission below it. It is difficult to estimate sizes for these features as they are barely resolved. If their distances from the minor axis represent true vertical distances above the plane, then these range from about 7 to 11 kpc. The fifth feature suggests a broken shell of diameter ∼4 kpc at the adopted distance. The features as they appear in the full-resolution cube are shown in Fig. 3.

3 NGC 5023 MODELS

For the modelling of the H I, we start with first estimates based on values found in the literature (PA, inclination, D_{25}, etc.) and derive the initial estimate for the rotation curve from a map of intensity weighted mean velocities through the GIPSY routine ROTCUR. This means that this initial estimate will underestimate the real rotation curve due to the edge-on orientation of NGC 5023 (Sancisi & Allen 1979). To obtain initial estimates of the surface brightness as well as a scaleheight, we compare averaged emission profiles in the vertical direction as well as the radial direction (see Fig. 4). It was found that the shape of the surface brightness profile is very well constrained by the GIPSY routine RADIAL. We use these initial estimates as input for TIRIFIC (Józsa et al. 2007) and let it fit the central coordinates. These central coordinates are then fixed in the fitting process but refitted for the final models to ensure their accuracy. All models have a velocity dispersion (including instrumental effects) of 10 km s^{-1} (van der Kruit & Freeman 2011, and references therein).

After fitting the central coordinates we proceed to fine-tune the initial parameters, through an iterative process in which fits by eye are alternated with χ^2 minimization with TIRIFIC, for a set of possible models. The fits by eye are always done by a comparison between the data and the model in several representations such as position–velocity (PV)-diagrams, moment maps, channel maps and radial profiles (shown in Figs 4–9). The final fit was always done by eye and subsequently confirmed by χ^2 minimization. For simplicity, we compare the models and the data in a coordinate system that is rotated by 62° such that the major axis of the central parts of the galaxy is aligned with the x-axis (as is the case in figures showing moment or channel maps). Once we obtain the best fit to the data by varying the position angle (PA), scaleheight, surface brightness profile and rotation curve, we investigate how the addition of other features, such as flares, line-of-sight warps and a lag influence the fit to the data. We always fit the approaching and receding side independently unless noted otherwise. For a more detailed description of the modelling process see Kamphuis et al.

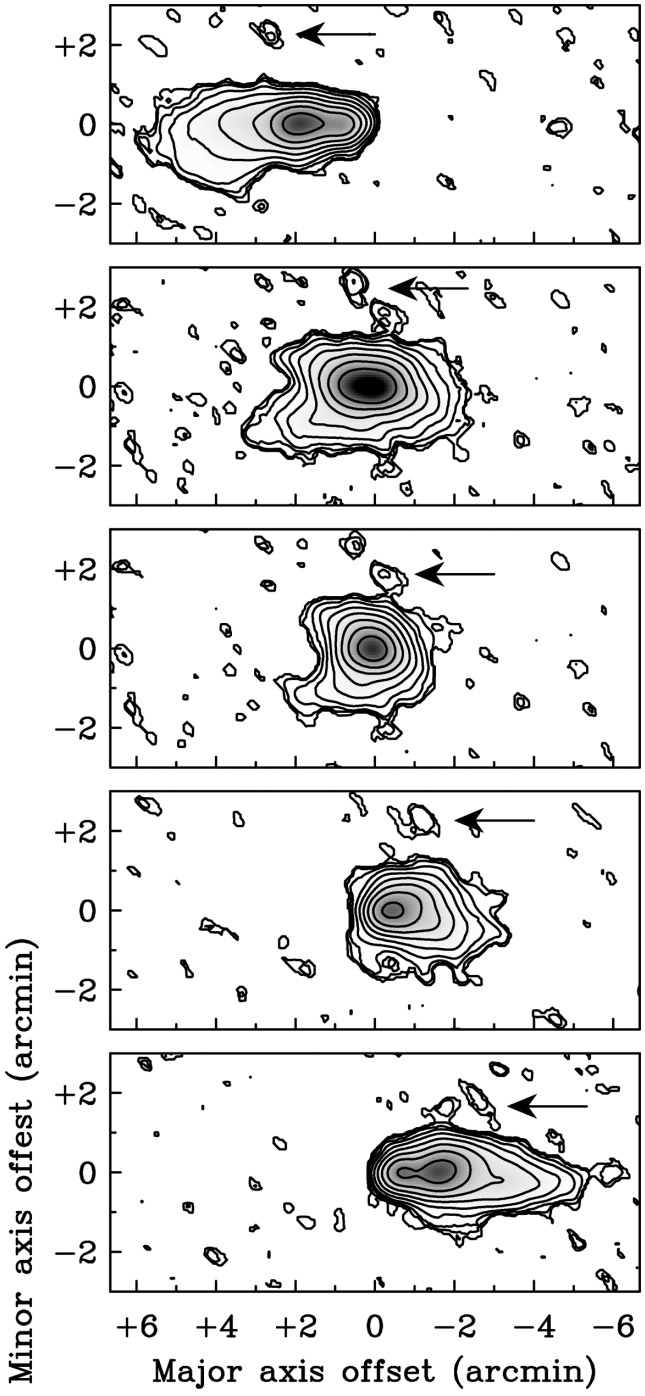

Figure 3. UGC 2082: zeroth-moment maps of the five features listed in Table 2 as seen in the full-resolution cube (top to bottom: Features 1−5). Limited velocity ranges have been used to isolate the features: they are 622−647 km s^{-1}, 667−724 km s^{-1}, 688−712 km s^{-1}, 721−741 km s^{-1}, and 750−778 km s^{-1} for Features 1–5, respectively.

(2011) and Zschaechner et al. (2011). We will describe the successes and failures of the individual models below.

3.1 Base model

This model is obtained by fine-tuning our initial estimates and will be used as the starting point for all the other models. In this model,

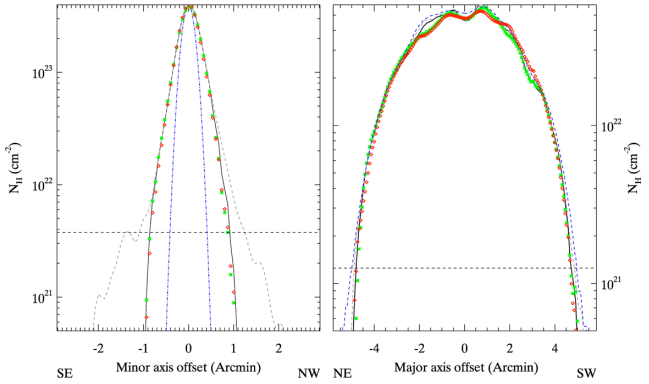

Figure 4. NGC 5023. Left: minor axis profiles of the data (grey dashed line), of the data without the areas where the residual is higher than 50 per cent (solid black line), base model (green asterisks) and the best-fitting spiral arms model (red diamonds) summed over the inner 300 arcsec in the radial direction. Right: same as the left but now with major axis profiles integrated over the inner 100 arcsec in the vertical direction. The blue dashed line shows the profile derived by the RADIAL task in GIPSY in the right-hand panel and a Gaussian with the FWHM of the beam in the left-hand panel. The horizontal black dashed lines indicate the lowest contour of Fig. 5.

we vary only the parameters that need to be varied in order to obtain a minimal satisfactory fit to the data. In the case of NGC 5023, this means that the surface brightness, the rotational velocities and the PA are required to vary per ring and the approaching and receding sides are fitted independently. In addition to these parameters that can vary from ring to ring, we also fit the inclination and scaleheight as a single parameter, i.e. constant for all rings. Fig. 4 shows the integrated major axis surface brightness profile of NGC 5023 (right-hand panel, solid black line) as well as the profile of the base model (green asterisks) and the RADIAL profile (blue dashed line) used as an initial estimate. The vertical profile (left-hand panel) shows a smoothly declining single exponential profile, with a second component at the higher offsets. However, as will be shown later on, this second component is entirely due to the individual features described in Section 2.2.1. Therefore, we forego fitting a double exponential or double Gaussian layer in our models (see also Zschaechner et al. 2011). With the exclusion of the warped area of the disc, the final parameters in this model vary less than 5 per cent from their initial estimates, implying that the methods used for obtaining these estimates are fairly accurate for flat discs.

The major axis profile in Fig. 4 shows a mismatch between the data and the model: the model underestimates the flux in the data around a radial offset ~ -100 arcsec. A zeroth-moment map (Fig. 5) shows that this is mostly due to the two large individual extra-planar features described in Section 2.2.1 (Features 2 and 3) that can never be captured in global axisymmetric models. We have confirmed this by comparing the central strip (20 arcsec wide) of the model to the data and indeed the discrepancy disappears. These features also cause the bumps seen at column densities $\sim 10^{22}$ cm^{-2} in the vertical profiles (Fig. 4, left-hand panel grey dashed lines). That these bumps are caused by the features can be seen from the difference between the grey dashed line, that includes all the data, and the solid black line, where the areas with a final residual, of the data minus the model, higher than 50 per cent are excluded. The bottom panel of Fig. 5 shows clearly that these areas are solely due to the described features. From Fig. 5, it also becomes clear that for a minimal satisfactory fit we need to vary the PA as the peak of the emission

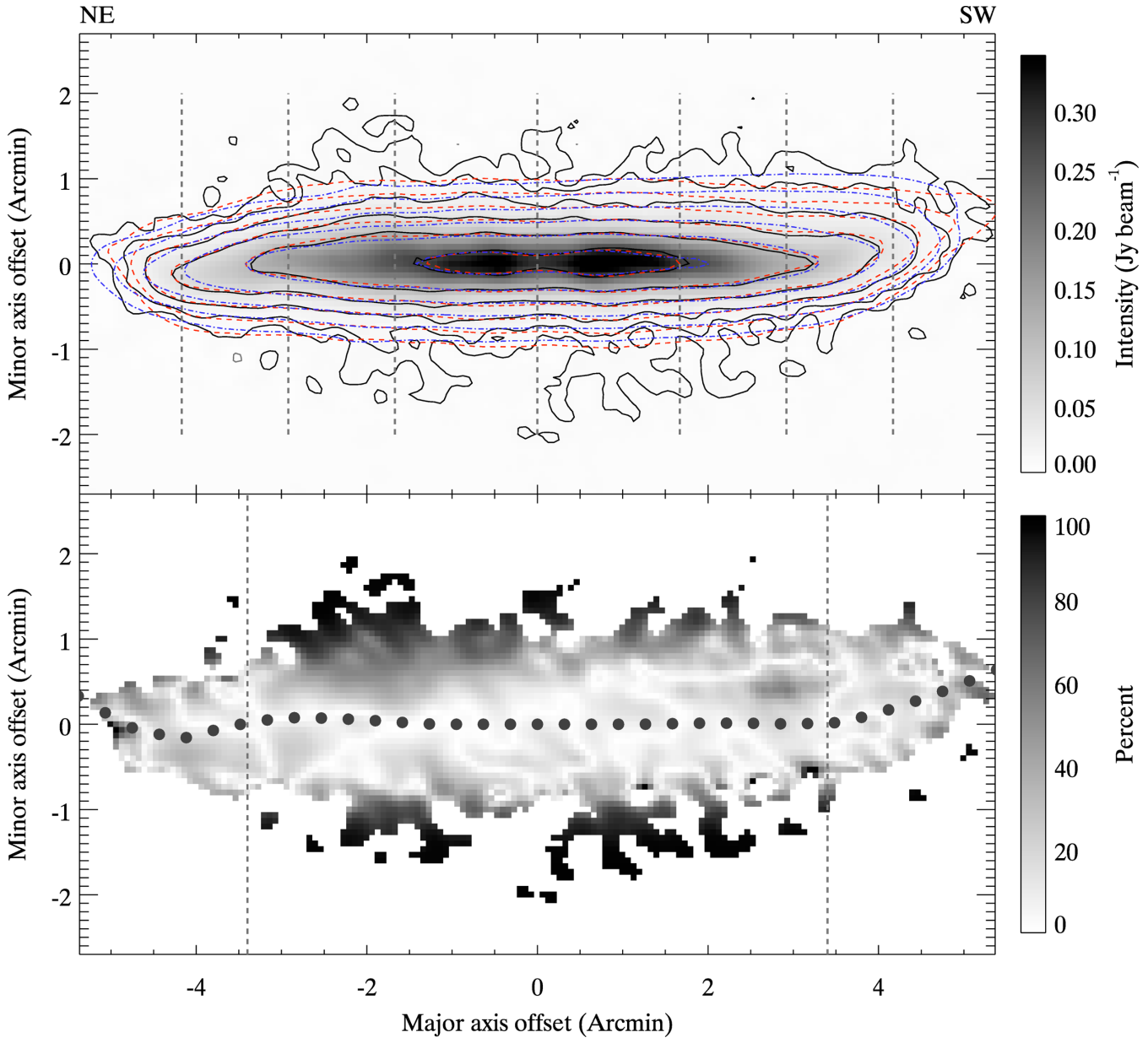

Figure 5. NGC 5023. Top: contours of integrated H I (black solid contours, grey-scale), the base model (red dashed contours) and the spiral arm model (blue dot–dashed contours) at high resolution. The contour levels are $2.5^n \times 2 \times 10^{19}$ cm^{-2}, $n = 1-6$. Vertical dashed lines indicate the locations of the slices presented in Figs 6 and 7 Bottom: residual map of the data and the spiral arm model in percentages of the observed flux. Vertical dashed lines indicate D_{25}. The dark grey symbols in the lower panel show the run of the PA in the base model.

at the outer radii bends away from the mid-plane. This run of PA is shown as circular dots in the bottom panel of Fig. 5 and shows that, even though the PA of all rings was fitted as a free parameter, the PA angle hardly varies within D_{25} (vertical dashed lines).

This model provides us with a best-fit surface brightness profile and rotation curve. Such a model fails to fit the data in several aspects. Fig. 6 shows PV-diagrams parallel to the minor axis at five different radial offsets. In these PV-diagrams, the data clearly show the triangular shape, outlined by the red dashed lines, that is indicative of a vertical gradient in the projected rotational velocities. However, in our simple model (second column) these triangular shapes are missing. Especially, the opening angle of the contours on the terminal side is much larger in this model. This behaviour is also recognized in the channel maps (not shown) furthest from the systemic velocity where the layer in the model is far too thick when compared to the data. This behaviour is seen throughout the galaxy and clearly indicates that the model needs a modification that causes lower projected velocities above the plane. Now we explore whether this can be reproduced with structural changes or only with changes to the kinematics.

3.2 Flare

One way of obtaining lower projected velocities above the plane could be by including a flare in the model. A flare can be seen as a central depression in the radial gas distribution which grows as

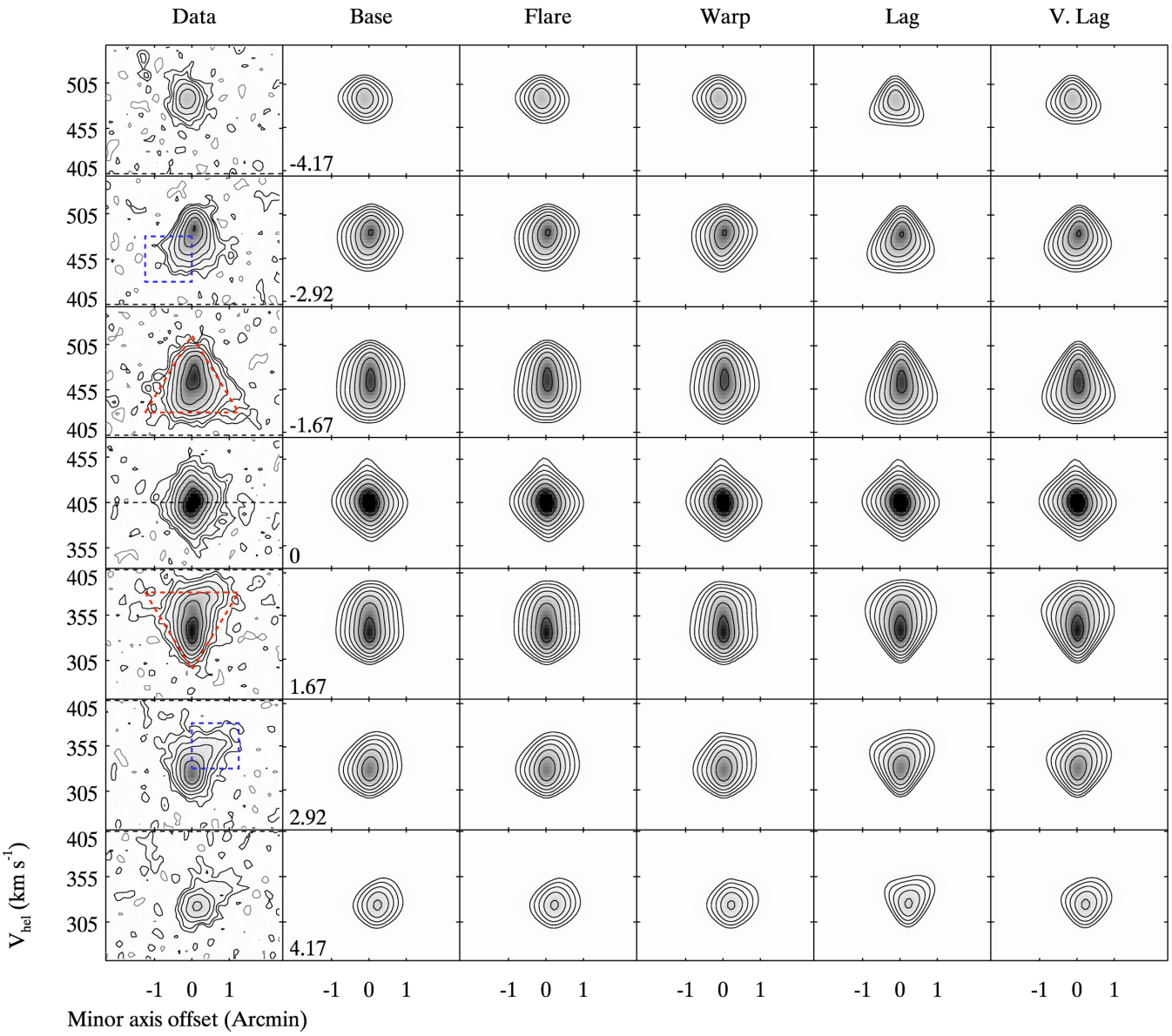

Figure 6. NGC 5023: representative PV-diagrams parallel to the minor axis at different major axis offsets (shown in each panel) for the data (left) and the various models. Contour levels are $2^n \times 1.5 \times$ the noise level of 0.19 mJy beam^{-1}, for $n = 1{-}7$ [negative $n = 1, 2$ (grey) is also shown]. The models are, from left to right, the base model, a flaring model, a model with a line-of-sight warp, a model with a vertical gradient and the last column shows a model with a vertical gradient that varies as function of radius. The red and blue dashed lines outline areas of interest which are used in the text to highlight differences between models. The horizontal lines show the systemic velocity.

one moves away from the mid-plane. This way, as one moves away from the mid-plane, less and less gas is detected on the line of nodes thus making it appear as if the rotational velocities are declining. In our modelling, a flare is simulated by increasing the scaleheight of the rings at larger radii. To construct a flaring model, we refit the scaleheights of all rings using once more a mixture of fits by eye and TIRIFIC. To ensure that we obtain the optimal flare model, we allow the other parameters to rescale as a whole. This resulted in a minimal change, compared to the base model, in the inclination (Δinc $= 0.^\circ02$).

Looking at the third column in Fig. 6, which shows the flaring model, we see immediately that the flare does not significantly improve the match between these models and the data. The flaring model has the same problems as the base model. As a flare would mean another set of free parameters and the fit does not significantly improve compared to the base model, we do not include a flare in our final modelling.

3.3 Line-of-sight warp

A second way to lower the projected line-of-sight velocities is to include a warp component along the line of sight. We can already see in the zeroth-moment map (see Fig. 5) that the outer radii of the disc are warped. This warp might be purely restricted to the plane of the sky; however, it is more likely that it is also partially along the line of sight. Such a warp can be included in the models by letting the inclination vary as a function of radius. Once more this would place gas at the outer radii above the plane thus leaving the line of nodes empty. The PV-diagrams of this model are shown in the fourth column of Fig. 6. In this case, the allowed rescaling of

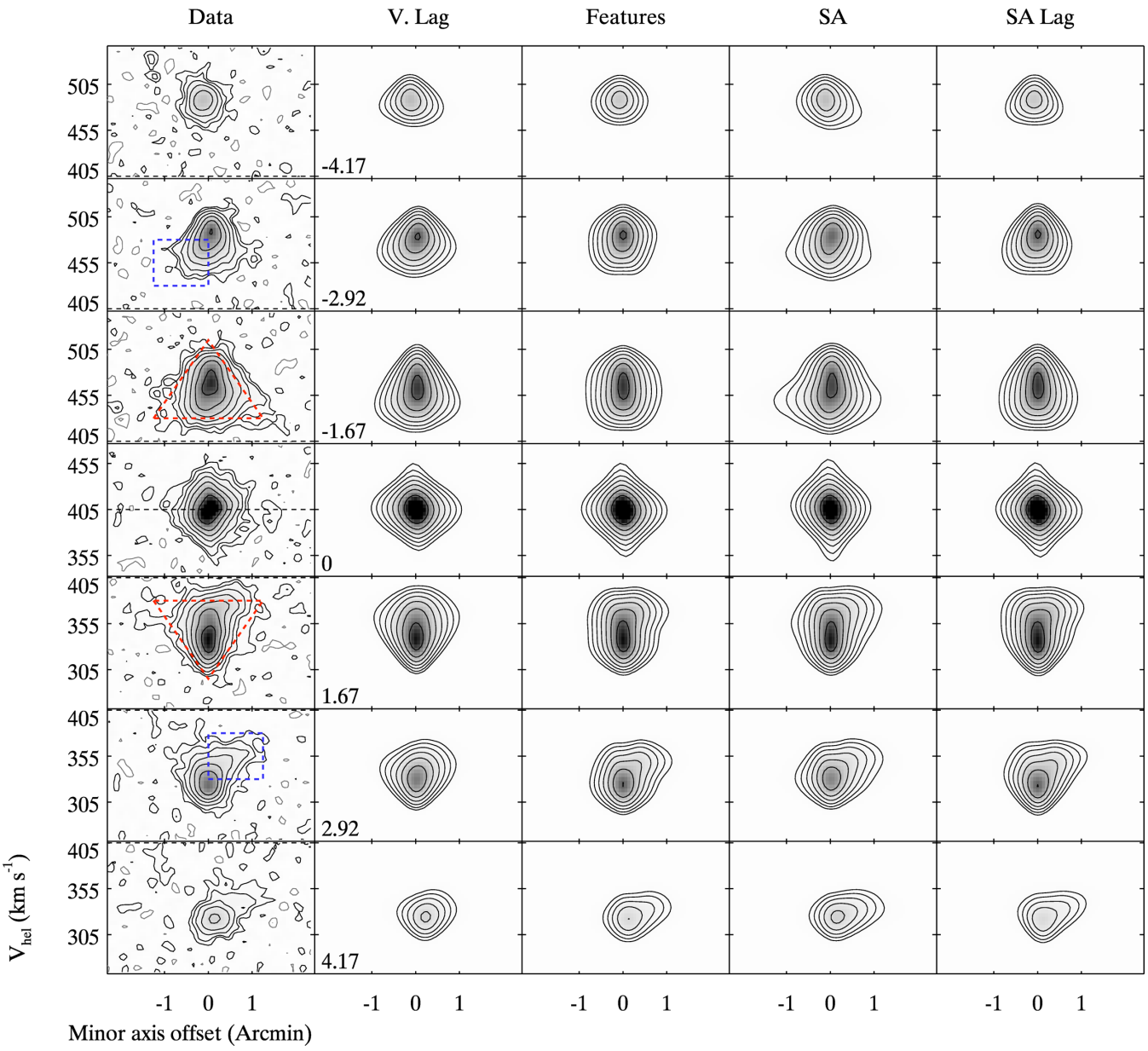

Figure 7. NGC 5023: as Fig. 6. The models are, from left to right, the 'classical' model with a radially varying lag, a model with partial discs added to it, a model with spiral arms added to the disc and the same model with a vertical gradient. The features model is described in Section 3.5 and the spiral arms models in Section 3.6.

the other parameters did not lead to a change in these parameters. Like the flaring model, this model does not significantly improve the fit to the data. Most importantly the triangular shape is still not matched in any of these PV-diagrams.

We also tried more extreme versions of a line-of-sight warp and flaring, i.e. ones that were not the best fit to the zeroth-moment map or radial/vertical intensity profiles, but none of these improve the shapes seen in the PV-diagrams enough to warrant the degradation of the fit to the density distribution.

3.4 Lag

The last global option to alter the velocities of the gas above the plane is not to rely on projection effects but to actually lower the rotational velocities as a function of distance above the plane. This model is shown as the second to last column of Fig. 6. It can be quite easily seen that of the models discussed so far this is the only model that actually shows the same overall shapes as the data in these PV-diagrams. The model shown in the figure does not include a flare or a line-of-sight warp thus maximizing the vertical gradient required to match the data. This model was chosen as it has the fewest free parameters and neither the flaring model nor the line-of-sight warp model, without a lag, significantly improve the overall fit to the data. However, in order to check quantitatively that the flaring model and line-of-sight warp model do not affect the determination of the vertical gradient in rotational speeds, a lag was fitted to all three models.

In order to obtain an objective estimate of the required vertical gradient in these models, we have fitted in two different methods. Once by TIRIFIC and once by measuring it directly in the model and the data. The estimate with TIRIFIC was done by approaching the lag with initial values on both sides of the expected value. As TIRIFIC

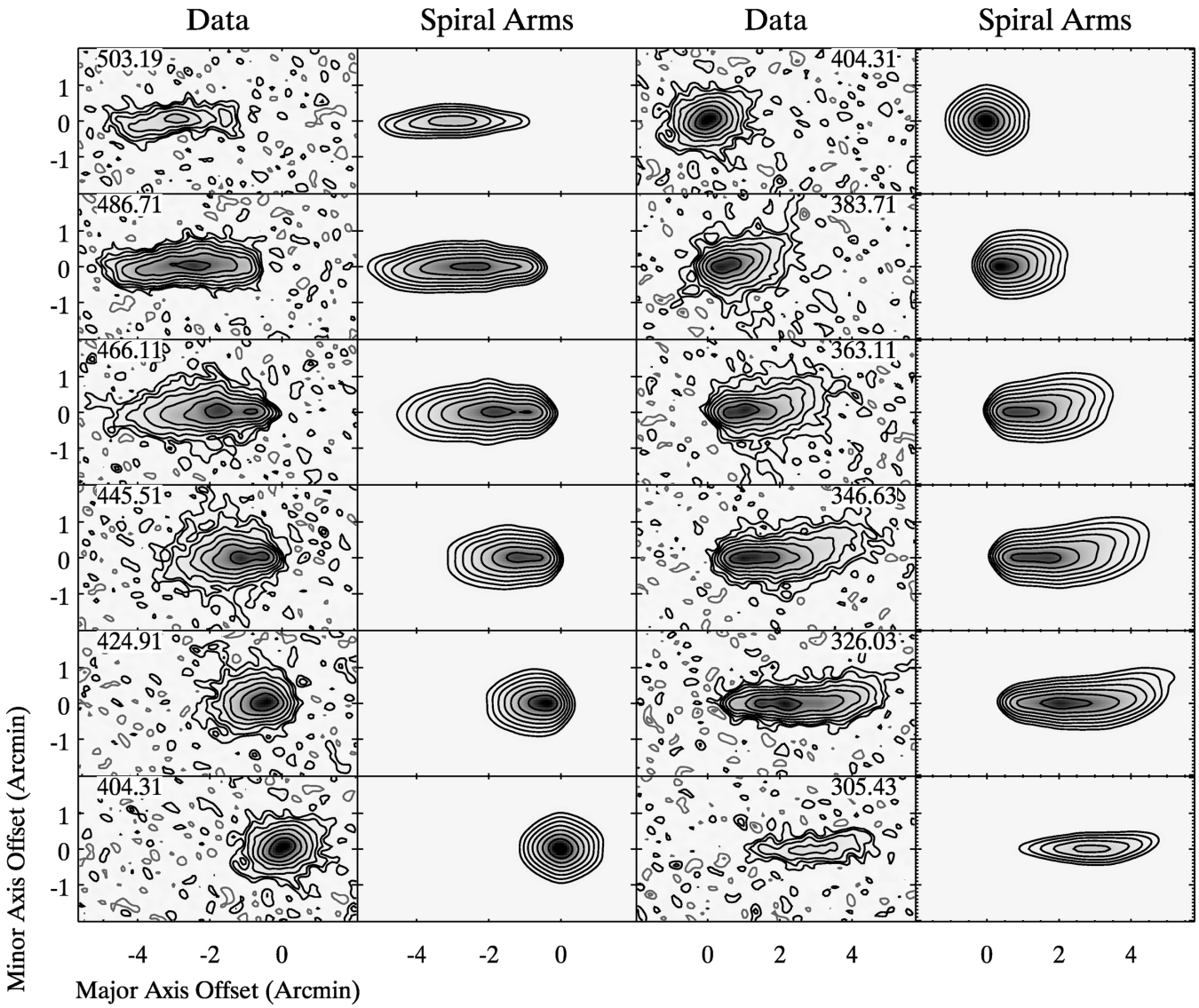

Figure 8. NGC 5023: representative channel maps in the rotated frame for the data and the best model ('spiral arms'). Contour levels are the same as in Fig. 6.

is used in the golden section mode, which fits local minima (see Józsa et al. 2007), the final value of the fit can differ depending on the initial input value. Therefore, the lag, and its error, was determined as the average of two TIRIFIC fits; one in which the lag was fitted starting from 0 km s^{-1} kpc^{-1}, and one where the starting point was -22 km s^{-1} kpc^{-1}. These lags are presented in Table 3. This table also provides the second method where the vertical gradient is measured in normalized PV-diagrams along the minor axis (see Kamphuis et al. 2007a, 2011). In such diagrams, every line profile is normalized by its maximum, and then the slope of maxima as a function of height above the plane is measured in the data and subsequently compared to the final model with a range of vertical gradients (e.g. 0–30 km s^{-1} kpc^{-1}). The vertical gradient is found as the gradient in the model where the measured slopes compare best to the slopes in the data. For NGC 5023, this slope was measured in the vertical range from $\pm$10–70 arcsec in strips 20 arcsec (30 arcsec for the low-resolution data) wide over a radial range of $\pm$50–150 arcsec. We see that the two methods are formally in good agreement but that measuring the slopes consistently gives higher values. Tests with measurements over different areas show that in general increasing the maximum height of the measurement range lowers the measured vertical gradient by roughly $\sim$0.2 km s^{-1} kpc^{-1} arcsec^{-1}. This means that this value is sensitive to the area we choose. Therefore, we will rely on the lags determined by TIRIFIC for the rest of our discussion as it fits the whole cube while accounting for the noise in the data.

From Table 3, it becomes clear that, if all we model are axisymmetric structures, models of NGC 5023 need a vertical a vertical gradient of $\sim -15 \pm 3$ km s^{-1} kpc $^{-1}$ in its rotational velocities. It also confirms our previous conclusion that the line-of-sight warp and the flaring models do very little to improve the fit to the PV-diagrams shown in Fig. 6. As these models do not significantly improve the fit, we conclude at this point that the base model with a vertical gradient of $\sim -15 \pm 3$ km s^{-1} kpc^{-1} is our superior approach in the 'classical' tilted ring analysis. However, there are still many discrepancies between the data and the model that resembles the data best.

As a last resort in our global models, we now try varying the lag in the model from ring to ring. This model is shown in the last column of Fig. 6. Such a variation has been found in other

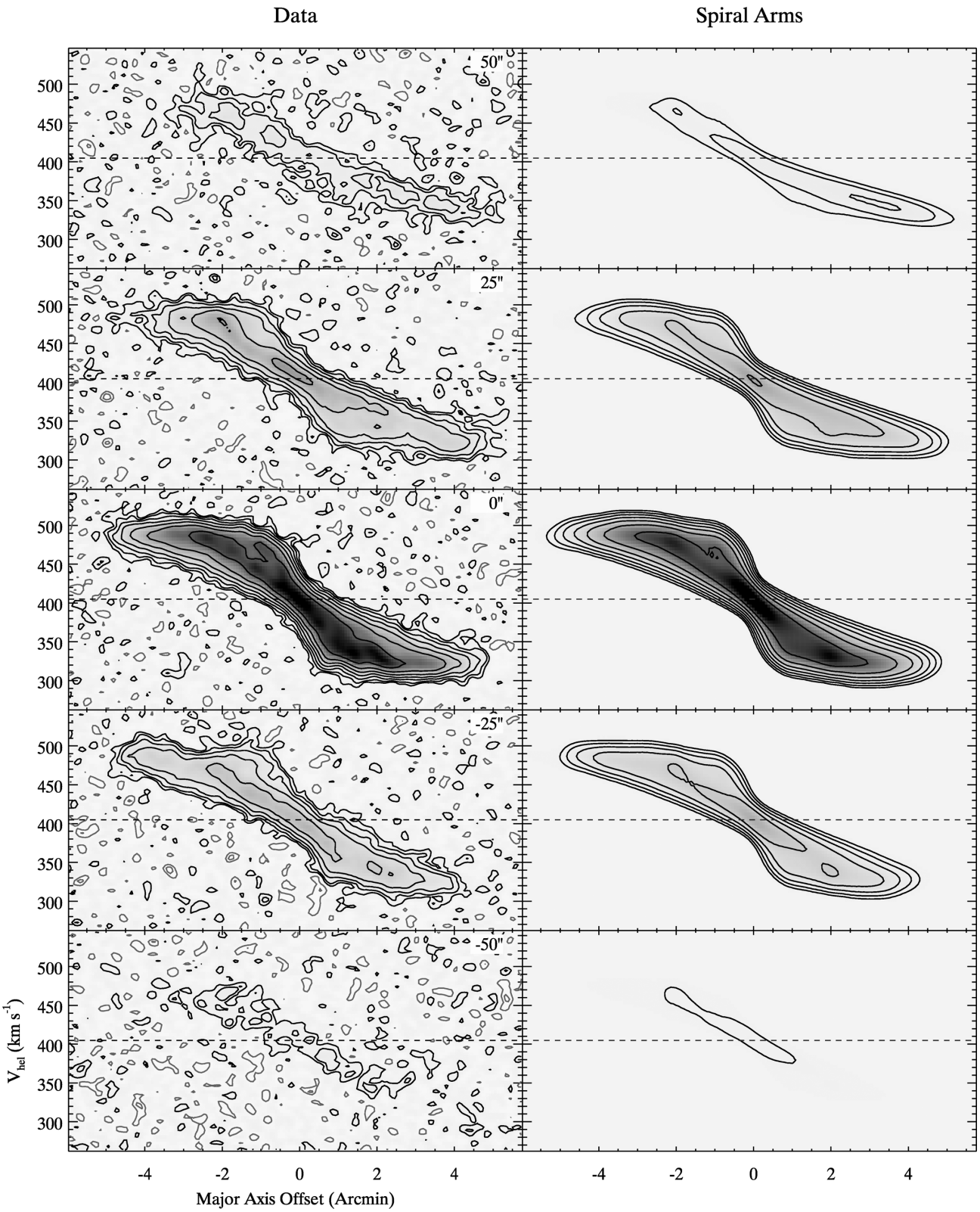

Figure 9. NGC 5023: representative PV-diagrams parallel to the major axis at different minor axis offsets (shown in each panel; positive offsets are to the north in the rotated frame) for the data (left) and the best model (right). Contour levels and dashed lines are the same as in Fig. 6.

galaxies (Oosterloo et al. 2007; Zschaechner et al. 2011, 2012) and if present in all galaxies it could provide us with important clues about the origin of the lagging gas. Additionally, an inspection of Fig. 6 clearly shows that the lag in our lag model is overestimated at the outer radii (i.e. the bottom and top row in Fig. 6). In order to investigate such a radial variation, we take two separate approaches. First, we take our final models with a constant vertical gradient and let TIRIFIC fit the gradient in each individual ring. This resulted in the

Table 3. NGC 5023: vertical gradients that are required for matching the models to the data for both the high-resolution data (FWHM = 19 arcsec × 13 arcsec) as well as the low-resolution data (FWHM = 36 arcsec × 33 arcsec). Left-hand column: name of the model. Middle column: vertical gradient as determined from fitting with TIRIFIC. Right-hand column: vertical gradient as determined from measuring the slopes of normalized PV-diagrams parallel to the minor axis.

Model	TIRIFIC lag ($km\,s^{-1}\,kpc^{-1}$)	Measured slope ($km\,s^{-1}\,kpc^{-1}$)
High resolution		
Base model	-14.9 ± 2.7	-17.9 ± 5.9
Flare	-15.3 ± 3.7	-16.3 ± 6.5
Line-of-sight warp	-14.9 ± 3.2	-17.4 ± 6.1
Spiral arms	-9.4 ± 3.8	-14.7 ± 8.2
Features	-5.4 ± 3.2	-10.9 ± 8.6
Low resolution		
Base model	-11.6 ± 6.6	-19.4 ± 3.9
Flare	-13.3 ± 6.2	-18.2 ± 4.2
Line-of-sight warp	-12.6 ± 5.4	-19.1 ± 4.0
Spiral arms	-7.9 ± 4.9	-15.4 ± 5.2
Features	-5.3 ± 5.3	-8.8 ± 5.1

Notes. Left-hand column: name of the model. Middle column: vertical gradient as determined from fitting with TIRIFIC. Right-hand column: vertical gradient as determined from measuring the slopes of normalized PV-diagrams parallel to the minor axis.

rings having some very different gradients. However, there was no clear radial dependence visible over all rings and the new models were no significant improvement over the models with a constant gradient for all rings. Secondly, we reduced the lag at the outer radii fitting the models by eye, consistent with previous findings of a radially varying lag (Zschaechner et al. 2011, 2012). This second method resulted in a lag that declines from $-14.9\,km\,s^{-1}\,kpc^{-1}$ at 133 arcsec (4.3 kpc) to $0\,km\,s^{-1}\,kpc^{-1}$ at 304 arcsec (9.7 kpc). This model improves the fit at the outer radii significantly and is considered at this point the best approach in describing the data.

With our 'classical' analysis, where all variations of the disc extend over half a cylinder, we have now found that the most likely explanation for the kinematics above the plane is a radially varying vertical gradient in the rotational velocities of the gas. Even though the vertical gradient declines to $0\,km\,s^{-1}\,kpc^{-1}$ at the outer radii, the PV-diagrams parallel to the minor axis (Figs 6 and 7) show that the opening angle of triangles is now too small, i.e. the lag appears too high. Additionally, the PV-diagrams show that at major axis offsets of 1.7, 2.9 and 4.2 arcmin there are extensions at mid- to high-altitude (vertical offsets between 0.4 and 1.3 arcmin) which are not reproduced by the model. These extensions are at low projected rotational velocities (V_{hel} 25 to 75 $km\,s^{-1}$ away from V_{sys}) and are outlined by the blue dashed boxes in Fig. 6. Similar extensions appear in the PV-diagrams at major axis offsets of -1.7 and -2.9 arcmin, albeit to a lesser degree, and on the other side of the disc (at V_{hel} 0 to 60 km^{-1} away from V_{sys} and vertical offsets between -0.4 and -1.3 arcmin). Clearly, they are extended structures in, or right above, the disc that are currently not reproduced by our global models.

3.5 Non-symmetric modelling

The current version of TIRIFIC allows us to add partial (i.e. of restricted azimuth range) discs to our models. This means that we can now construct features in our models which cover only a small part of the total disc and that have parameters that differ from the underlying axisymmetric disc. This enables us to investigate the effect of localized features on our global analysis. The data already suggest that the extra-planar gas in NGC 5023 is far from cylindrically symmetric and therefore we think this galaxy is an excellent opportunity to test this next step in tilted ring modelling. As discussed before, when the density distribution of the extra-planar gas differs significantly from that in the disc, this can mimic a vertical gradient due to gas missing at the line of nodes.

As a proof of concept, we try to model the individual features first by adding a partial disc to each side (i.e. approaching and receding) of the final models of the previous sections. These discs are limited to a maximum azimuthal extent of 90°, i.e. a quarter disc, and are restricted to follow the rotation curve and PA of the final model of the previous section. However, we refit the radial surface brightness profile and the scaleheight of the model. We also fit the scaleheight, surface brightness profile, azimuthal extent and azimuthal centre, i.e. the PA of the feature in the face-on view, of the new discs. As it is likely that small variations in inclination can now severely affect our results, the inclination is treated in a special manner. The rings with radii larger than 175 arcsec are fitted independently from each other whereas the rings at smaller radii are fitted with a single value. In this we always require the inclination for the partial disc to match that of the full disc at any given radius, i.e. the partial disc is oriented in the same way as the full disc. Here, the fitting process is once more a mixture of χ^2 minimization with TIRIFIC and fits by eye. The approaching and receding sides are fitted independently.

Fig. 7 shows that adding partial discs to the base model causes a significant improvement immediately. The peculiar extended features seen in Fig. 6 at mid-altitude and low rotational velocities are now clearly reproduced on the south-western side of the disc, i.e. positive radial offsets. However, the triangular shapes in the PV-diagrams parallel to the minor axis that are normally associated with a lag are still not defined very well. When we fit a lag for this model in the same way as for the global models, we find that the need for a lag is significantly lowered. Even though the best-fitting lag is still non-zero, a model without a lag cannot be excluded anymore (see Table 3). However, when we view this model from a face-on perspective, it becomes clear that it is very unphysical. The left-hand side of Fig. 10 shows this face-on view, which is created by taking the absolute value of the model's inclination in each ring and subtracting 90°. From this viewing angle, it is clear that certain parts of the disc are much brighter. By giving these parts a different scaleheight [$z_{disc} = 8.9, 7.6$ arcsec (0.28, 0.24 kpc) versus $z_{feature} = 26.1, 15.7$ arcsec (0.84, 0.50 kpc)] for the negative and positive offsets, respectively] and adding a line-of-sight warp, the density distribution above the plane is significantly different from that in the plane of the galaxy. Fig. 10 also shows that the fitting process has pushed the partial discs as far as possible from the line of nodes, therefore minimizing the need for a vertical gradient. However, as is easily seen from Fig. 10, this is not a very realistic distribution of the gas.

3.6 Spiral arms

Since the appearance of the model in the left-hand panel of Fig. 10 does not resemble typical real galaxies, we try to reproduce the effect while constraining the additional discs to resemble logarithmic spiral arms. We apply the same constraints as in the case of the partial discs but with the additional restrictions that the width and phase angle of the additions follow a smooth distribution that resembles two independent spiral arms. This smooth distribution

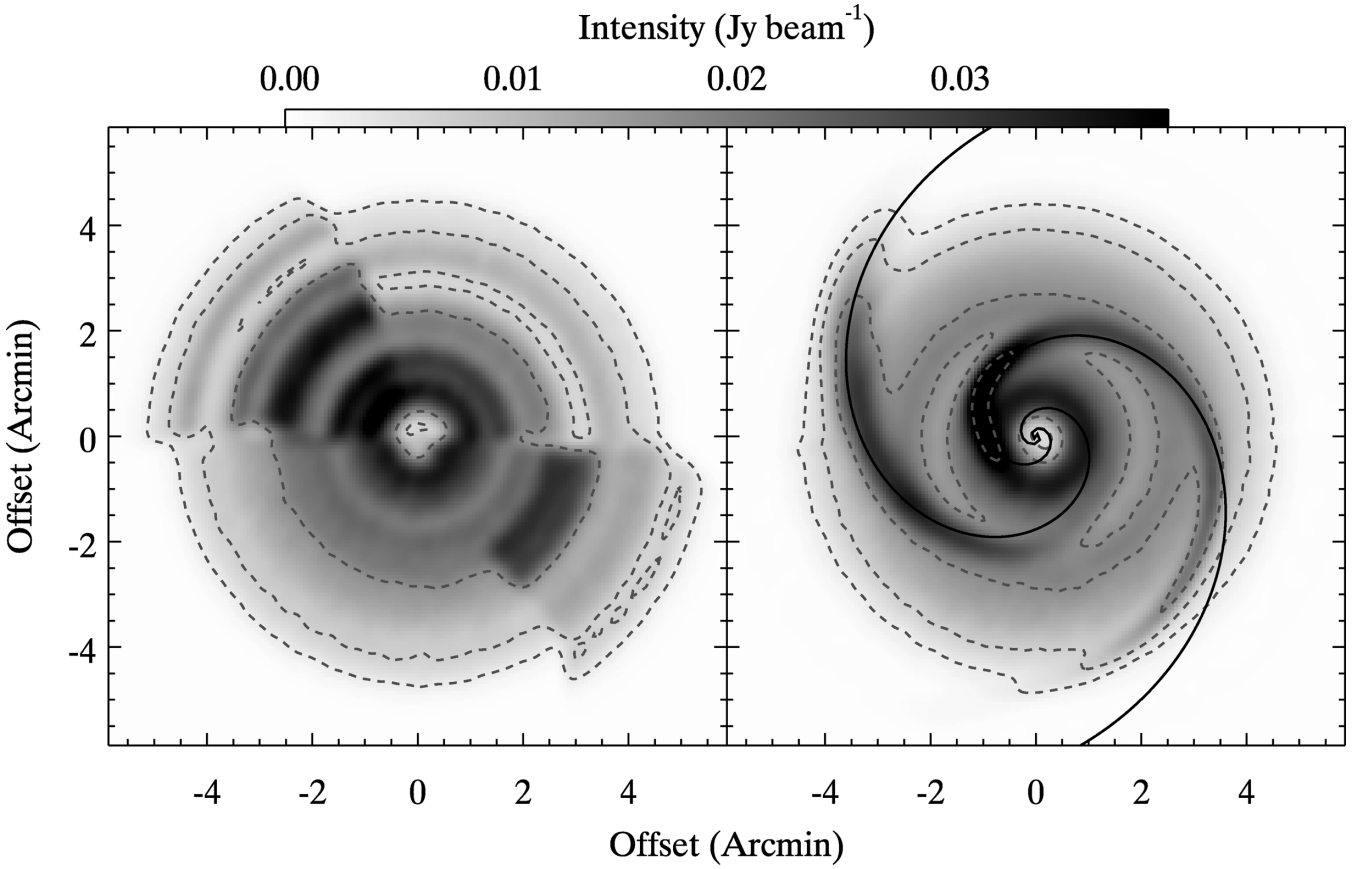

Figure 10. NGC 5023: face-on zeroth-moment map of the model with partial discs added (left) and spiral arms (right). The contour levels are $2.5^n \times 2 \times 10^{19}$ cm^{-2}, $n = 1-4$. The black lines in the right-hand side map represent a logarithmic spiral arms with a pitch angle of 22° following the orientation of the disc. The normal line of sight is along the x-axis with the observer on the right-hand side.

is achieved through manual regularization. The initial best guess phase angles are calculated such that two perfect identical logarithmic spiral arms with a pitch angle of 20° are added to the model. This is somewhat below the typical value for galaxies with rotational velocities similar to NGC 5023 (Kennicutt 1981). During the fitting, the only constraint on this phase angle is that the changes from one ring to the other are smooth (see Fig. 11), i.e. we do not enforce logarithmic spiral arms. The phase went through several, both manual and TIRIFIC, iterations before arriving at this final solution. Another difference in the fitting process is that we refit the PA in a similar manner to the inclination. This is because spiral arms can imitate warping behaviour when the inclination deviates from exactly edge-on (Byrd 1978). For this reason, we may already be interpreting some spiral structure as PA variations in e.g. the base model.

The PV-diagrams of the best-fitting spiral arms model also successfully reproduce the low-velocity high-altitude features outlined by the blue boxes in Figs 6 and 7 and now, when seen face-on, we have a much more realistic distribution of the gas (see Fig. 10, right-hand panel). The face-on view also shows that the added individual structures still roughly follow the shape of logarithmic spiral arms, albeit the pitch angle has changed to ∼22° (black lines in Fig. 10), which is still low for this type of galaxy (Kennicutt 1981). Additionally, the underlying disc is now fully cylindrically symmetric except for PA and inclination (see Fig. 12), thus significantly reducing the complexity of the models. However, comparing the opening angles of the model contours in Fig. 7 to those of the data, it is clear that the model still requires a lag. This is confirmed by fitting the lag with TIRIFIC in the same way as for the classical' models (see Section 3.4). This way we find that this best-fitting model still requires a vertical gradient of -9.4 ± 3.8 km s^{-1} kpc^{-1}. Additionally, we once more investigate the presence of any radial dependence in the vertical gradient but for these models the improvement is insignificant and therefore we discard such models as they add another set of free parameters. However, we would like to point out once more that such a variation does seem to be present when comparing the models to the data. The prime example of this can be seen in the PV-diagram with a 4.2 arcmin offset shown in Fig. 7.

Since the assumption of spiral arms is physically motivated and the addition significantly improves the fit to the data, we deem the spiral arm + lag model to be the best fit to data. It must be noted that in this model it is crucial to have a radial variation in the inclination in the disc, i.e. a line-of-sight warp, to fit the extended low-velocity high-altitude structures. Also, the best-fitting scaleheight of one of the arms deviates from that of the disc and the other arm (see Fig. 11, Table 4). Without these changes, especially the warp, the improvement compared to the base model would not be significant. In order to determine which of these parameters is the dominant effect on the lag, we refitted the lag for two models: one with the scaleheight of the arms fixed to the scaleheight of the disc and one where the inclination of the disc and arms was kept constant at the central value. When the scaleheights were fixed this resulted in a lag very similar to the best fit ($dV/dz = -8.8 \pm 2.5$ km s^{-1} kpc^{-1}). However, when the line-of-sight warp was removed the lag ($dV/dz = -14.5 \pm -3.1$ km s^{-1} kpc^{-1}) was found to be very similar to the final 'classical' model. This confirms that

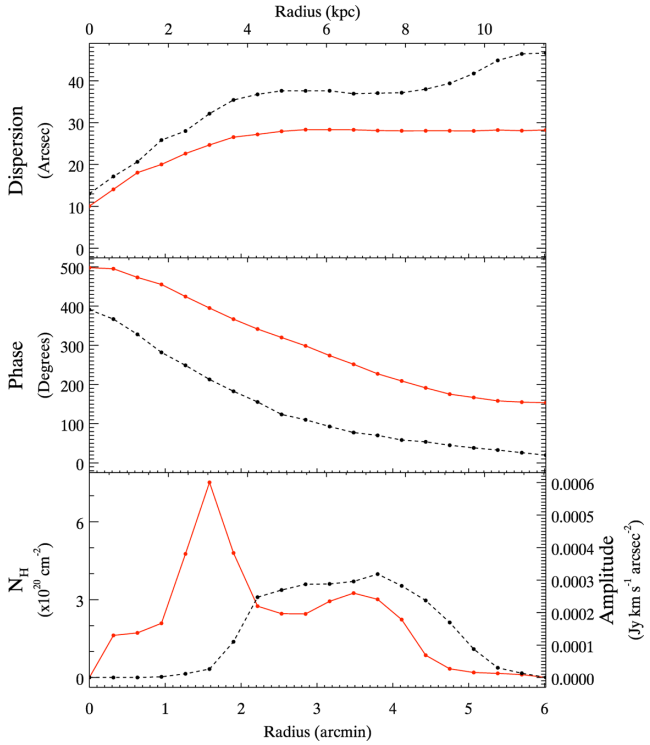

Figure 11. NGC 5023: parameters of the arms in the best-fitting model with spiral arms, with from top to bottom: the dispersion of the overdensity/arm, i.e the width in each ring, the phase, i.e. the central position of the overdensity in each arm and the amplitude of the overdensity/spiral arm. The black dashed line and the red solid line show the parameters for the two arms.

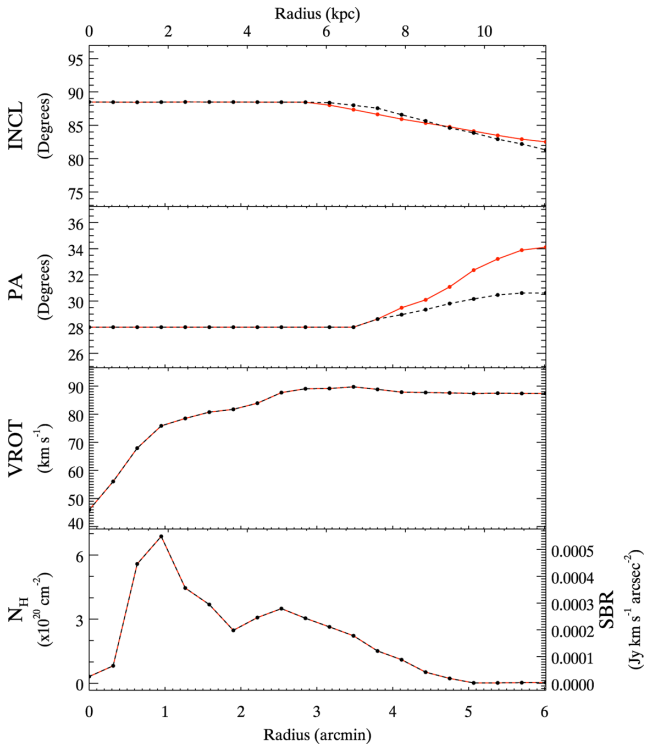

Figure 12. NGC 5023: parameters of the disc in the best-fitting model with spiral arms. The black dashed line is for the approaching (SW) side, this line is missing for the bottom two panels as the discs are the equal. The red solid line for the receding (NE) side.

in the case of NGC 5023 the lowered lag is due to the presence of the arms in the line-of-sight warp.

It is difficult to provide errors on the different values of the various components of the model, especially when each ring is allowed to vary independently. This is because many of the parameters are degenerate at some level. In the individual rings, the matter is even worse as often the value of each ring is slightly degenerate with its neighbouring rings as well. However, in order to provide some estimate of the error on each parameter, we have systematically varied each parameter of the best-fitting model, while keeping the others fixed, until the model and data clearly deviated. If during this process, when lowering the parameter, a value in a single ring became less than zero it was set to zero. The central best-fit parameters and their errors determined this way are presented in Table 4. The stated errors are the average maximum allowable deviation found when increasing and decreasing the parameter's values. Because Table 4 provides the central values of all parameters it sometimes appears as if the error is larger than the value; however a quick look at Figs 11 and 12 shows that this is not the case for the majority of the rings.

The addition of spiral arms introduces a large number of extra parameters to the model. Additionally, we are trying to fit structures that are actually only indicated in the velocity structure of our data and that are normally only visible in face-on galaxies. With 20 rings in each disc of the model, we introduce 122 [Z0 (2), arm amplitude (40), phase centre (40), arm dispersion (40)] new free parameters to the model by introducing the spiral arms. Of these, 80 are correlated in the sense that ring to ring changes should be smooth; therefore, large jumps are smoothed in the model.

Counting each ring as a free parameter should be considered a simplistic attempt to quantify the number of free parameters in the models. Often user interaction will reduce the freedom of a parameter such that it should not be considered a truly independent parameter. Additionally the number of rings used for the model can also vary, using smaller ring sizes would result in more rings to vary and thus in more free parameters in our estimation. However, their spacing would be less than a beam and therefore neighbouring rings would be much more correlated than in the current model. Another uncertainty in the number of rings is introduced by the edge of the disc, which is not observed. In the case of NGC 5023, we choose to model the galaxy up to the minimum radius that fully includes the 2σ contour in the low-resolution cube ($\sim$6 arcmin). However, one could argue for more rings, as the edge appears to be undetected, or less rings, as the data become severely affected by the noise.

Following the simple approach outlined above, the total number of free parameters for our final model then becomes 206 [Z0 (1), DVRO (1), SBR(20), VROT(20), PA (21), INCL (21),[3] Spiral Arms]. When we compare this to the commonly accepted 'classical' two-disc modelling, we have significantly increased the number of free parameters, as in such a model we would end up with 126 [SBR(40), VROT(40), PA (40), INCL (2), Z0 (2), DVRO (2)] free parameters. However, the inclusion of common variations such as a radially varying lag, a flare, a free central position, a line-of-sight warp or a two-component vertical disc would quickly increase the number of free parameters to our spiral arm model. Additionally, we can see in Fig. 12 that the differences between inclination on both sides of the disc are minimal. Another thing to keep in mind is that the models are still severely oversampled as a conservative estimate give us $\sim$1300 resolution elements (based on an independent area of emission of 250 arcsec $\times$ 100 arcsec every three channels) in the

[3] The inner 10 rings of the disc are fitted as a single value for the inclination and PA, as described previously in the text.

Table 4. NGC 5023: parameters of the best-fitting model and their errors. Except for the mass (total flux) and the rotational velocity (velocity at $D_{\rm H\,I}$) the central values are reported.

Parameter	Disc	Arm 1	Arm 2
Centre (α J2000)	$13^{\rm h}12^{\rm m}11.83^{\rm s} \pm 4.3^{\rm s}$		
(δ J2000)	$44^\circ 2' 16.9'' \pm 6''$		
$V_{\rm sys}$ (km s^{-1})	404.8 ± 4		
Inclination ($^\circ$)	88.5 ± 1.3		
PA	28.0 ± 1		
$V_{\rm rot}$ (km s^{-1})	87.6 ± 5		
Scaleheight (arcsec)	9.1 ± 3	14.0 ± 9	9 ± 6
Scaleheight (kpc)	0.29 ± 0.10	0.45 ± 0.29	0.29 ± 0.19
Mass ($M_\odot$)	$4.8 \pm 0.26 \times 10^8$	$4.9 \pm 0.7 \times 10^7$	$4.3 \pm 0.3 \times 10^7$
Dispersion (arcsec)		13 ± 23	10 ± 25
Phase centre ($^\circ$)		390.8 ± 7.5	497.9 ± 7.5

high-resolution cube. Therefore, we deem the increase of free parameters in the model acceptable, especially as specific features in the data can only be reproduced when such non-cylindrically symmetric overdensities are introduced to the model and spiral arms are a well-documented feature of face-on galaxies.

It is remarkable to see how well the shapes of the initial logarithmic spiral arms are maintained (see Fig. 10) by the simple condition that the phase angle and width should only vary smoothly, even though their actual pitch angle has changed by almost 2° in the fitting process. Although it must be said that the characteristics of the arms are ill constrained (see Table 4).

In general, there are three firm conclusions to take away from the modelling:

(i) NGC 5023 requires non-axisymmetric overdensities in its gas distribution. For these overdensities to significantly improve the fit, the disc needs to be slightly warped in the line of sight.

(ii) NGC 5023 requires a vertical gradient in its rotational velocities.

(iii) In NGC 5023, the value of the vertical gradient is affected by the specifics of the non-cylindrical distribution.

4 UGC 2082 MODELS

We turn to the isolated, low-SFR edge-on UGC 2082. Contours of H I emission from the full-resolution cube are shown in Fig. 2. From an initial examination presented in Heald et al. (2011), it was already clear that the H I emission was extended in the minor axis direction, and a PV-diagram parallel to the minor axis suggested that a line-of-sight warp is largely responsible. The zeroth-moment map also suggested a warp component across the line of sight. The minor axis extent was noted to be greater on the approaching (SE) side of the galaxy, particularly evident on the S quadrant on that side. Some high-latitude extensions were also seen on the NE side of the disc. The total H I mass detected is 2.54×10^9 $M_\odot$, which agrees well with that measured from single-dish observations of 2.4×10^9 $M_\odot$ (Springob et al. 2005). Small-scale, isolated features at the first contour level in Fig. 2 represent noise peaks and are not significant.

Here, we attempt to understand the distribution and kinematics of the H I by modelling the emission in the full-resolution cube. Once more, the modelling essentially follows the standard techniques used for HALOGAS galaxies, using primarily TIRIFIC to create model data cubes, although some details vary from the procedure used for NGC 5023. Initial estimates for the systemic velocity and dynamical

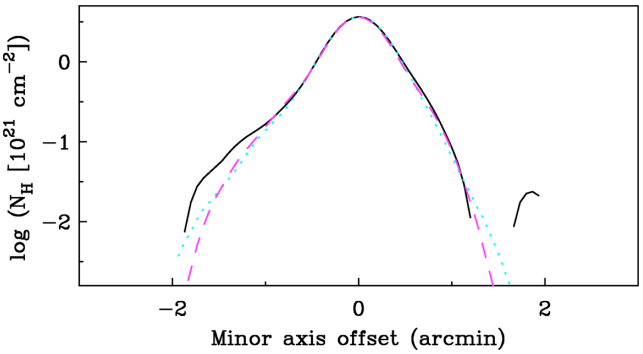

Figure 13. UGC 2082: minor axis profiles averaged over the central 5 arcmin along the major axis for the data (solid black line), base warp model (dotted cyan line) and best model (dashed magenta line). Other models (not shown) fit the data about as well but are rejected for other reasons (see the text).

centre, and dependence of the major axis PA on radius were made from the GIPSY program ROTCUR. The initial estimate for the rotation curve and radial surface density profile is derived from an initial automated fit to the data cube using TIRIFIC. Inclinations near 90° are considered initially. The vertical density dependence of modelled layers is described by an exponential. A velocity dispersion is also specified.

No subsequent automated fitting was done for this galaxy. These parameters may all be manually refined by comparison of models and data through average profiles parallel to the minor axis, zeroth-moment maps, representative channel maps and PV-diagrams parallel to the minor and major axis, presented in Figs 13–18. Many models can be rejected using a minimum of such figures – zeroth-moment maps and PV-diagrams parallel to the minor axis most clearly reveal their deficiencies – hence those models will only be shown in those figures for simplicity. We work in a coordinate system where the galaxy has been rotated clockwise by 42° so that the major axis is horizontal in the moment and channel maps, with the approaching side on the left, and the NW side referred to as the N side in what follows. Given the clear asymmetries in this galaxy, all four quadrants were modelled independently unless otherwise specified. There are only slight deviations in the rotation curves and radial surface density profiles among the models considered; hence, we will present these only for the preferred model. The systemic velocity is 705 km s^{-1}, the dynamical centre is at RA $2^{\rm h}36^{\rm m}16\overset{\rm s}{.}6$, Dec. 25° 25′ 20″, and the velocity dispersion (found to match the

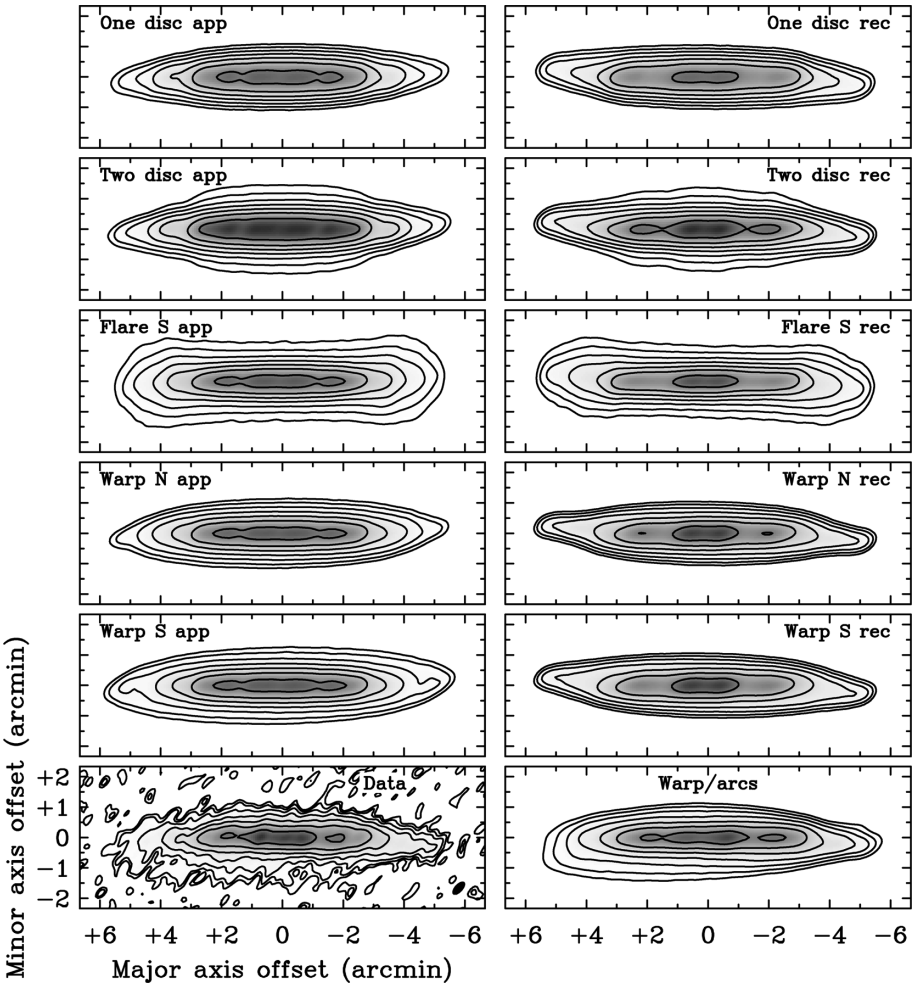

Figure 14. UGC 2082: zeroth-moment maps for the various models described in the text and for the data in the rotated frame where the major axis of the unwarped part of the disc is horizontal. The approaching side is at positive major axis offsets. In this and subsequent figures, labels 'N', 'S', 'app' and 'rec' refer to models that are optimized for the North, South, approaching or receding sides, respectively. 'Warp' refers to the line-of-sight warp in those models. Contour levels are $2^n \times 5.1 \times 10^{19}$ cm^{-2}, $n = 0{-}6$.

falloff of the contours on the terminal side of the PV-diagram along the major axis in Fig. 18) is 10 km s^{-1} in all models (with the exception of a few central rings in the final model, to be discussed later), with no significant change with height.

The zeroth-moment map (Fig. 14) of the full-resolution cube suggests a warp component across the line of sight. The aforementioned minor axis extension is still most prominent in the southern approaching (left) quadrant but some low-level, extended emission is apparent in the northern approaching and southern receding quadrants as well. The PV-diagrams parallel to the minor axis (Figs 15 and 16) show that this emission is found near the systemic (top of each panel on the approaching side, bottom on the receding side) end, at distances within about 4 arcmin along the major axis from the centre, with velocities moving towards systemic with increasing minor axis offset, while being rather narrow in velocity extent. As mentioned above, this appearance suggests a warp component along the line of sight is primarily responsible, although we will see that such a model cannot explain the high-latitude emission completely.

All models feature a warp across the line of sight. Initially, models featuring (a) a single, unflared disc, (b) two such discs with differing scaleheights (to search for a thick disc), (c) a single flared disc and (d) a single disc with the addition of a line-of-sight warp component were created and optimized by eye to fit the data.

4.1 Single-disc models

For the single-disc case, separate models were created for the approaching and receding sides rather than for all four quadrants. Only combinations of inclination (86–90° and scaleheight (11.5–15 arcsec or 800–1050 pc) that provided a good match to the averaged minor axis profile (Fig. 13) were considered. This model can be quickly ruled out from its appearance in the PV-diagrams parallel to the minor axis in Figs 15 and 16. In panels for major axis offsets at 3 arcmin or less from the centre, compared to the data, there is too great a vertical extent on the terminal end relative to the systemic end. No combination of scaleheight and inclination alleviates this problem while still providing a good match to the minor axis profile. The model also cannot reproduce the shape of the high-latitude extensions.

4.2 Two-disc models

The two-disc models begin with the single-disc models and add a thicker disc, constrained to have the same parameters as the thin disc but with a larger scaleheight. Various scaleheights were experimented with, but these models can quickly be ruled out by inspection of the PV-diagrams parallel to the minor axis (Figs 15 and 16). Particularly evident in the 2-3 arcmin panels, much of the

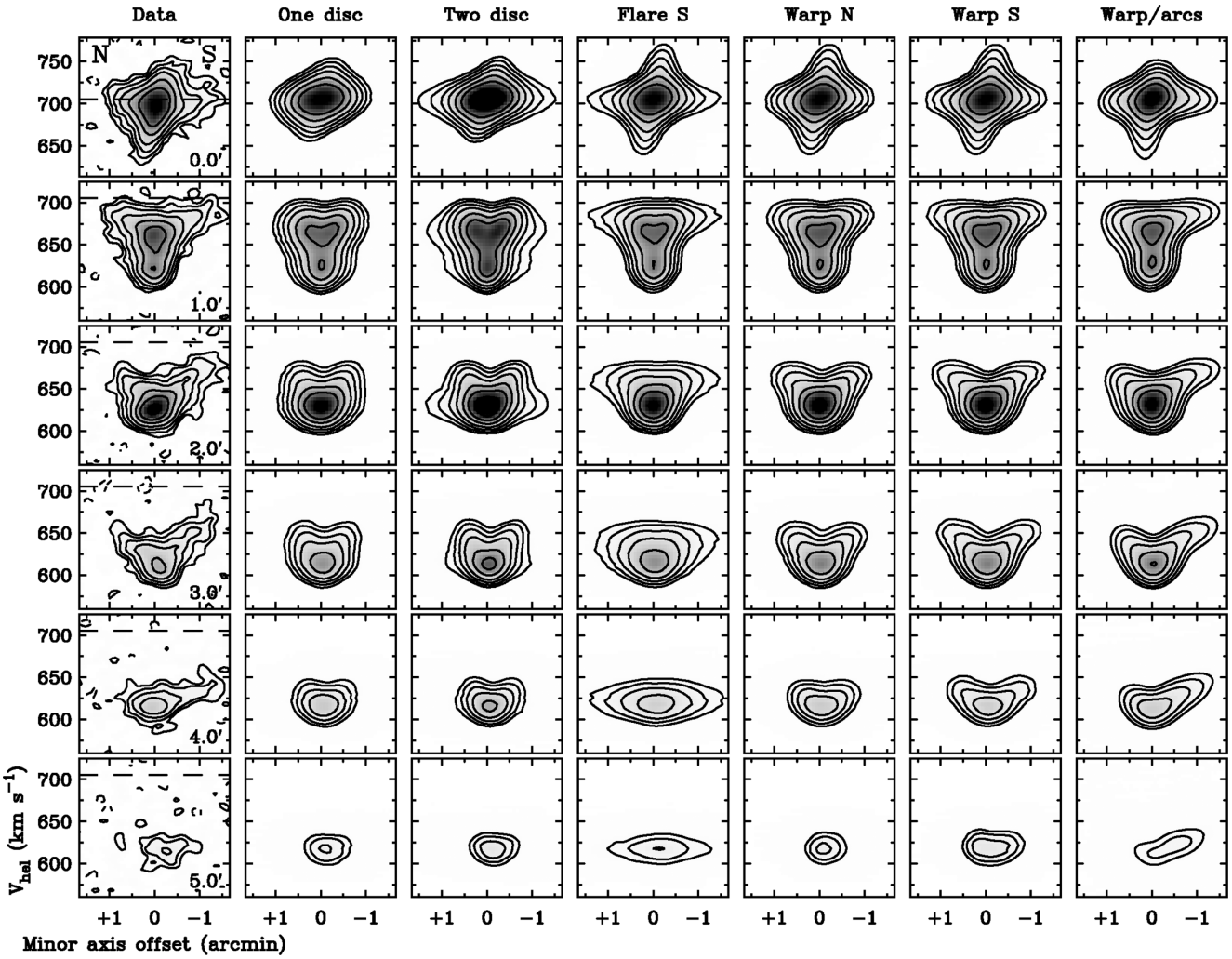

Figure 15. UGC 2082: representative PV-diagrams parallel to the minor axis at different major axis offsets (shown in each panel) for the data (left) and the various models for the approaching side (as well as the minor axis). Dashed lines in the data panels indicate the systemic velocity. Contour levels are $2^n\times$ the noise level of 0.21 mJy beam^{-1}, $n = 1-7$ (negative $n = 1$ also shown for the data).

high-latitude emission occurs at velocities close to the terminal velocity end, whereas more is needed at the systemic end. No variation of the parameters of this model will remove this generic deficiency. Given these failures, no attempt was made to optimize these models for each quadrant independently.

4.3 Flare models

In the flare models, the scaleheight of the unflared inner disc is 6 arcsec and the inclination is 84.°5 in all rings. All four quadrants are modelled independently, but only results for the south side will be shown, as this is sufficient to demonstrate the inadequacies of these models. The flare begins at $R = 3$ arcmin (approximately R_{25}) in all quadrants, but the increase of the scaleheight with radius varies among quadrants, with the most extreme rise in the southern approaching quadrant, where it rises linearly to 56 arcsec at $R = 6$ arcmin, and the least extreme in the northern receding quadrant, where the scaleheight increases to 12 arcsec at $R = 3.7$ arcmin and stays constant thereafter. These dependences allow the minor axis profile to be optimally fitted, but the generic failure of these models does not depend on the details of the inner radius of the flare or its severity. These failures are demonstrated by the zeroth-moment map and the PV-diagrams parallel to the minor axis. In the former (Fig. 14), the models generally fail to reproduce the tapering of emission with increasing major axis offset. In the latter (Figs 15 and 16), they are a particularly bad match to the data in the 3–5 arcmin panels, producing high-latitude emission with too broad a velocity width at velocities too close to the terminal end in the 3 arcmin panels, and overestimating the minor axis extent in the 4–5 arcmin panels.

4.4 Line-of-sight warp models

The model with a warp along the line of sight is more successful. Different scaleheights and dependences of the inclination with radius were experimented with until an optimal match was found to the channel maps and PV-diagrams while still fitting the minor axis profile well. The inclination of the unwarped disc is 84.°5−85°, and the line-of-sight warp begins at about $R = 200$ arcsec (again close to R_{25}). The warping is initially to smaller inclinations, reaching 78°–79°, depending on the quadrant, but on the receding side improvement was found by again increasing the inclination back to near 88° at major axis offsets >4.5 arcmin [otherwise the width of the emission in the channel maps (Fig. 17) at these offsets is

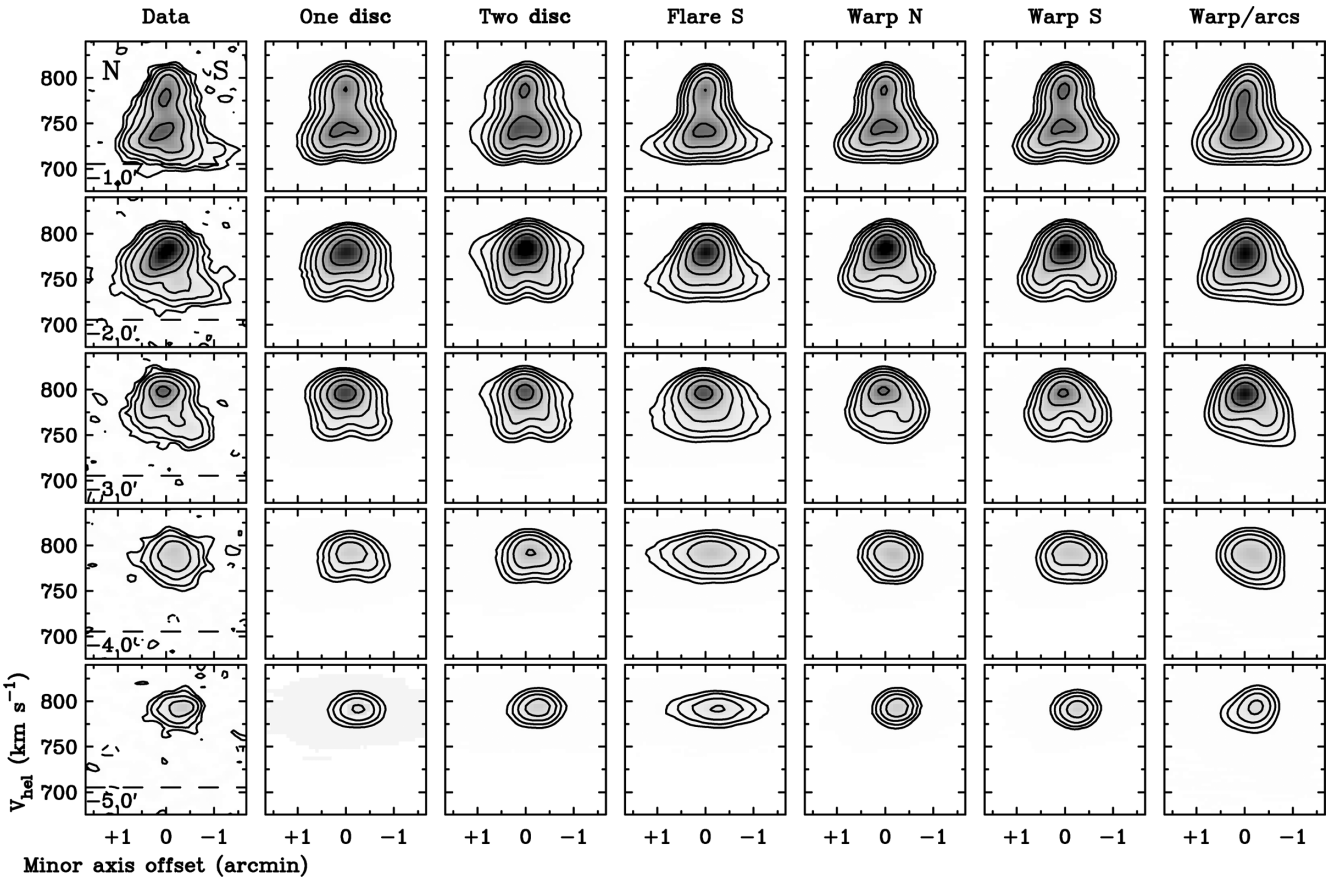

Figure 16. UGC 2082: as Fig. 15 but for the receding side.

clearly overestimated]. We do not discuss the run of inclination in this model any further as it is not the optimal model, although a simplified version of it is incorporated in our preferred model which is discussed in more detail later. Despite the improvement over the other models, this model suffers from several inadequacies. First, as for all models, different parameters in all four quadrants are necessary to fit the high-latitude extensions, as is clear in the PV-diagrams parallel to the minor axis (Figs 15 and 16). This raises doubts as to whether a line-of-sight warp component by itself is well motivated to explain these features. Secondly, the shape of the PV-diagrams parallel to the minor axis on the receding side in the 1–3 arcmin panels (Fig. 16) is still not well reproduced. In the 1 arcmin panel, the contours on the N side for the data are much straighter than in the model, and the high-latitude extension on the S side is poorly matched. In the 2 arcmin panel, the shape of this high-latitude extension is again poorly reproduced (also true in the 3 arcmin panel), and emission is underestimated at velocities $>750\,\mathrm{km\,s^{-1}}$ and minor axis offsets >30 arcsec on the north side. Thirdly, for the approaching side PV-diagrams parallel to the minor axis (Fig. 15), especially at 2, 3 and 4′ arcmin offsets, the southern minor axis extensions are also poorly matched, with the data showing more extended low-level emission. These inadequacies are also reflected in model channel maps (not shown).

4.5 Modeling the major asymmetries

Summarizing so far, all except the warp model can be clearly rejected, but that model cannot be made to reproduce the minor-axis-extended, asymmetric emission. Given this asymmetry, we next attempt to augment the warp model using TIRIFIC's ability to model rings of restricted azimuthal (in the plane of the galaxy) extent. The warp model we begin with is for the N side, separately optimized for the approaching and receding sides. The zeroth-moment map suggests that we should add a feature that is most noticeable in the S approaching quadrant, but we find that it must also extend into the S receding quadrant. A PA slightly larger and inclination slightly lower than values for the unwarped main disc, and an azimuth range that concentrates it along the southern side, yield such a feature that is most prominent in this quadrant. The arc must be placed at relatively large radii, as the PV-diagrams parallel to the minor axis (Figs 15 and 16) show that this extension is concentrated at the systemic end. We experimented with radial density profiles, as well as (assumed not to vary among rings in the structure) rotation velocities, inclinations, PA and vertical extents (we assumed a constant density with height). A second feature was added to the N half in order to reproduce the straightness of the contours in the 1 arcmin panel at minor axis offsets of 0.5-1 arcmin in Fig. 15 to add needed emission at the terminal end at these offsets in the 2 arcmin panels. Parameters were varied in the same way as for the first component to produce the best fit. Given the velocities and minor axis offsets at which this feature appears, it is necessarily at lower radii than the first arc, but with a large vertical extent. Both arcs were assumed to be concentric with and have the same velocity dispersion as the main disc.

We note here that we also attempted to fit these features with spiral arms as in our model of NGC 5023, but we found these models to be a poor match to the data.

We attempted to keep the base warp model as symmetric as possible, but slight changes were made. Removing the warp across the

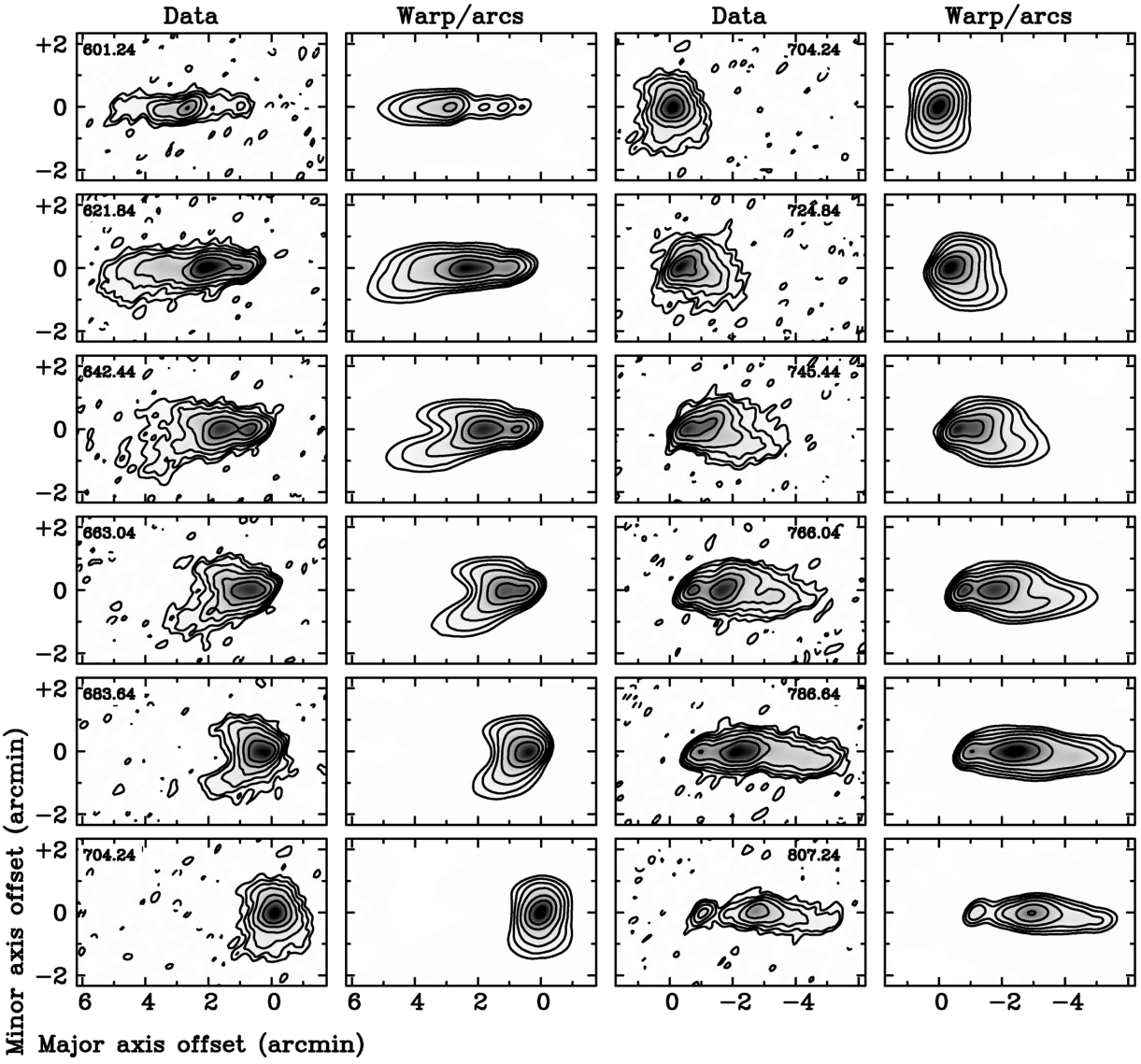

Figure 17. UGC 2082: representative channel maps in the rotated frame for the data and the best model ('Warp/Arcs'). Contour levels are the same as in Fig. 15.

line of sight on the approaching side resulted in slight improvements – hence, the downward bend of the emission towards the end of this side is solely due to the first added component. The warp along the line of sight is also now slightly less severe on this side. On the receding side, the aforementioned behaviour of the warp across and along the line of sight is still needed to reproduce the data. The velocity dispersion within 50 arcsec radius from the centre has been increased to 25 km s^{-1} to better match the high-velocity width in the minor axis slice (top row in Fig. 15) at minor axis offsets <30 arcsec. This value does not necessarily represent an actual increased dispersion – it could reflect poorly resolved non-circular motions near the centre of the galaxy. No other variations in velocity dispersion were found to be necessary to model, and no discrepancies between data and models indicated that radial motions would improve the fit.

The radial variation of parameters for the base warp model is shown in Fig. 19, while Fig. 20 shows the radial column density profiles for the two arcs (the deviations from a single column density for each arc do provide improvement to the quality of the fit). Table 5 lists the other parameters for the arcs. The channel maps and PV-diagrams parallel to the major axis for the data and this model are compared in Figs 17 and 18, respectively. A face-on view of the surface density distribution of the base warp model and the two arcs is shown in Fig. 21 (note the unavoidable discontinuities in the base model where the approaching and receding sides meet), and a view of the arcs alone from the observer's perspective in Fig. 22. Also note that Fig. 21 assumes that the S side of the galaxy is the near side. There is no prominent dust lane in UGC 2082 which could help break this ambiguity. The total H I masses are 6.8×10^7 and 1.3×10^8 M$_\odot$ for the N and S arcs, respectively.

The zeroth-moment map (Fig. 14) shows how the addition of these arcs produces a good match to the H I morphology. The PV-diagrams parallel to the minor axis (Figs 15 and 16) show how the first arc approximately reproduces the high-latitude tails at the systemic end in the 1−4 arcmin panels on both sides. The match is not perfect: for instance, on the approaching side, the emission in the data is slightly more extended along the minor axis, and the slope of the extension in the 4 arcmin panel on this side and the 2 arcmin panel on the receding side is shallower than in the model. The addition of the second arc has largely solved the aforementioned problems in this figure that motivated its inclusion. The

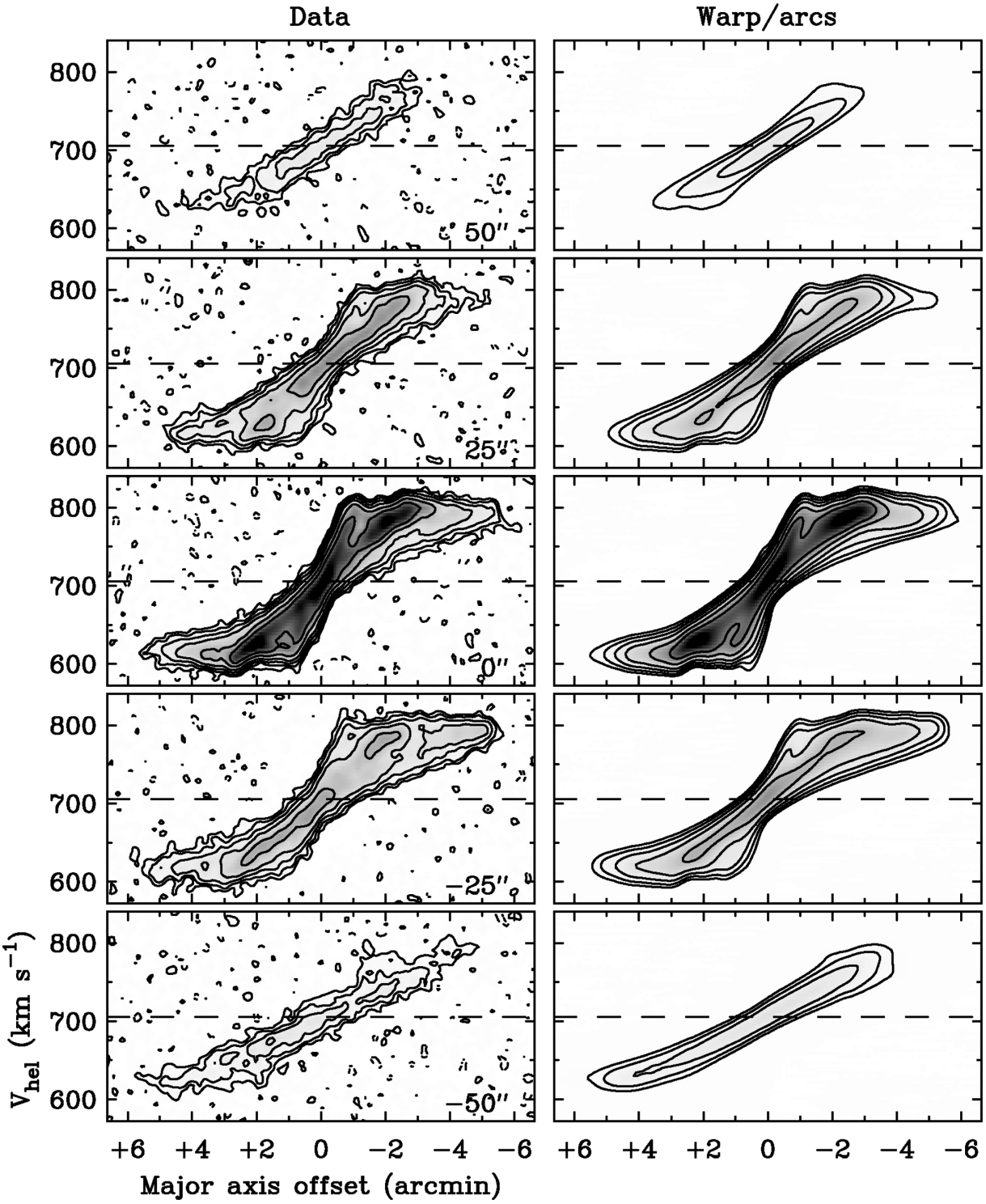

Figure 18. UGC 2082: representative PV-diagrams parallel to the major axis at different minor axis offsets (shown in each panel; positive offsets are to the north in the rotated frame) for the data (left) and the best model (right). Dashed lines in the data panels indicate the systemic velocity. Contour levels are the same as in Fig. 15.

channel maps (Fig. 17) and PV-diagrams parallel to the major axis (Fig. 18) also show excellent agreement, although a few isolated discrepancies are clearly noticeable.

When fitting by eye, it is difficult to assess the uniqueness of the arc parameters, but, as we did for NGC 5023, we can make estimates by varying parameters in turn while keeping the others fixed, and judging when the models cease to be good fits to the data. The error bars in Table 5 result from this exercise. The velocity dispersion of the S arc is uncertain by about 2 km s^{-1}, but that of the N arc is poorly constrained.

Following the discussion for NGC 5023, by including the arcs the number of free parameters in the model is not increased greatly.

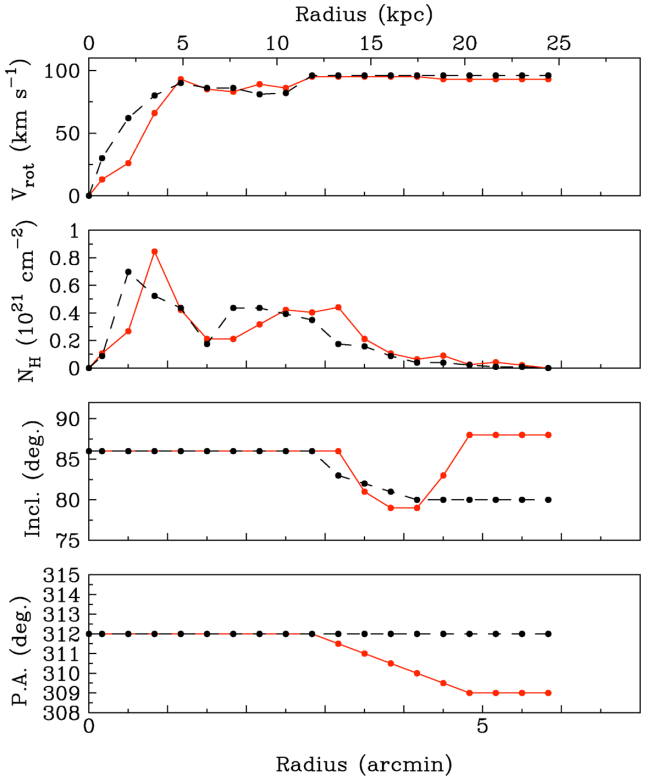

Figure 19. UGC 2082: parameters for the best base warp model for the approaching (dashed black lines) and receding (solid red lines) sides. From top to bottom are shown the rotation curve, column density perpendicular to the disc, inclination and PA versus radius.

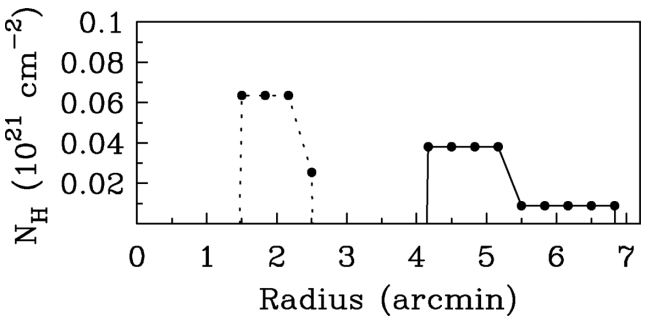

Figure 20. UGC 2082: column density perpendicular to the disc for the N (dotted) and S (solid) arcs versus radius.

Apart from the six parameters listed in Table 5 for each arc, no more than two distinct column densities per ring were experimented with (as reflected in 20), although variations in the central radius and width of the rings were also examined. Hence, effectively only 20 free parameters were added to the base warp model, which itself has almost 100 free parameters.

Beyond the features listed in Table 2, no additional small-scale or low-level emission was found in an examination of the full-resolution cube. The favoured model provides a reasonable fit to the 30 arcsec cube and no significant modification of the parameters is required.

Finally, we note that no lag is required in the fitting. There is no residual characteristic lag signature in Figs 15 and 16 of the type seen in NGC 5023 that would necessitate its inclusion. It should be recognized, however, that the linear resolution perpendicular to the disc ($\sim$ 1.5 kpc) is worse than in other edge-ons (350−900 pc; Oosterloo et al. 2007; Kamphuis et al. 2011; Zschaechner et al. 2011, 2012) where lags have been measured. It is therefore possible that higher resolution mapping could reveal a lag relatively close to the mid-plane.

Table 5. UGC 2082: parameters for the disc and two arcs. The disc inclination and PA are for the unwarped region. The disc and arcs have the same dynamical centre and systemic velocity. The disc rotation speed is an average value for the flat part of the rotation curve beginning at 3 arcmin radius. Δz is the vertical extent of each arc. AZ_0 is the central azimuth in the plane of the galaxy, with 0° being the approaching side of the major axis. ΔAZ is the azimuthal extent of each arc in the plane of the galaxy. The final row gives the per cent of the H I mass of the galaxy accounted for by each arc.

	Disc	N arc	S arc
Centre (α J2000)	$2^h36^m16.6^s$		
(δ J2000)	25°25′20″		
V_{sys} (km s^{-1})	705		
Incl. (deg.)	86	78 ± 5	78 ± 1.5
PA (deg.)	312	312 ± 3	316 ± 2
V_{rot} (km s^{-1})	95	85 ± 5	85 ± 5
Δz (arcsec)		40 ± 5	20 ± 5
AZ_0 (deg.)		255 ± 10	90 ± 10
ΔAZ (deg.)		205 ± 10	170 ± 10
Mass ($M_\odot$)		$6.8 \pm 1.7 \times 10^7$	$1.3 \pm 0.3 \times 10^8$
Mass (per cent)		2.7 ± 0.7	5.1 ± 1.2

5 DISCUSSION

5.1 NGC 5023 and spiral features

Through extensive modelling of the H I observations of NGC 5023 we have shown that this galaxy most likely contains spiral arms, but definitely some kind of non-axisymmetric gas distribution. This is the first time that such models have been created for an edge-on galaxy in order to investigate its effect on the observed vertical gradients in rotational velocity. We have seen that in a 'classical' analysis of the lag in NGC 5023 the vertical gradient would be $\sim -15 \pm 3$ km s^{-1} kpc $^{-1}$ up to a radius of 133 arcsec (4.3 kpc) and then decline to 0 at 304 arcsec (9.7 kpc). As this best-fitting model is without global line-of-sight effect, i.e. a line-of-sight warp or flare, this vertical gradient can be considered an absolute upper limit on the vertical gradient in NGC 5023. However, if we include non-axisymmetric features in the form of spiral arms, the vertical gradient derived from the best-fitting model would be lower (-9.4 ± 3.8 km s^{-1} kpc $^{-1}$) and constant with radius. Although there are indications in the data that a radial variation is present, including such a variation no longer improves the model fit significantly.

The fact that non-cylindrical distributions of the gas above the disc could severely affect the measurement of the vertical gradient has been known for a long time. However, until now it was impossible to accurately model such a distribution. With the improved capabilities of TIRIFIC we can now construct models that match the data to an unprecedented level of accuracy. Even though this increases the range of possible models that can be investigated, it also introduces a large set of new free parameters to the models. This means that any additions to the 'classical' two-disc cylindrical symmetric models should be motivated physically as well as improve the fit to the data significantly before they can be accepted as the better model.

Although the spiral arms in our model of NGC 5023 may have a slightly different scaleheight than the disc, their thickness is not

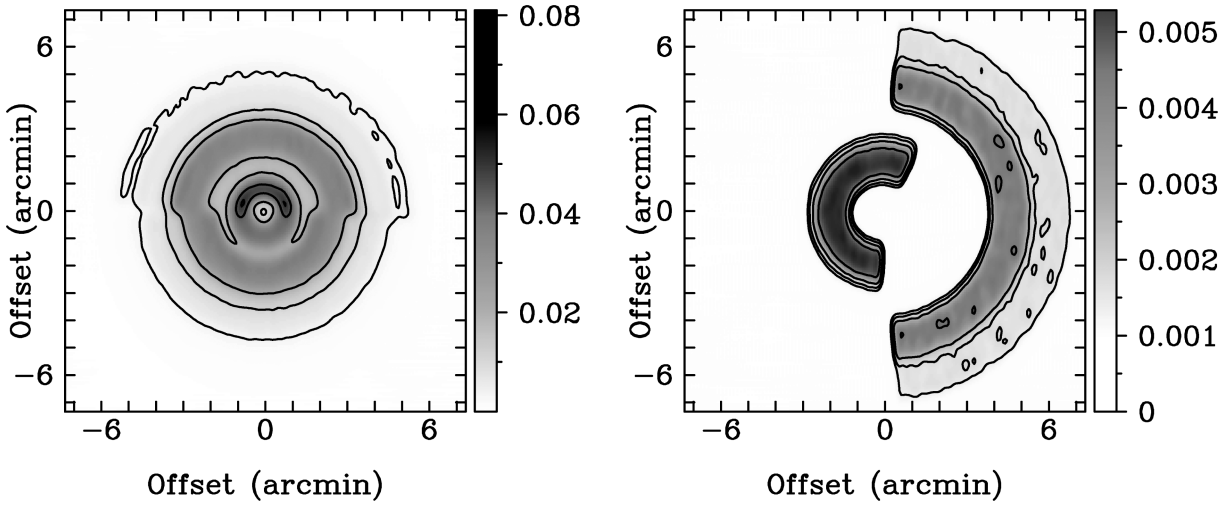

Figure 21. UGC 2082: the column density of the base warp model (left) and arcs (right) from a face-on perspective (with respect to the unwarped part of the base warp model). The models are observed from the right (the S side in the rotated frame of Fig. 14 is assumed to be the near side). Contour levels are $2^n \times 5.1 \times 10^{19}$ cm^{-2}, $n = 0{-}4$ for the disc, and $2^n \times 5.1 \times 10^{18}$ cm^{-2}, $n = 0{-}3$ for the arcs.

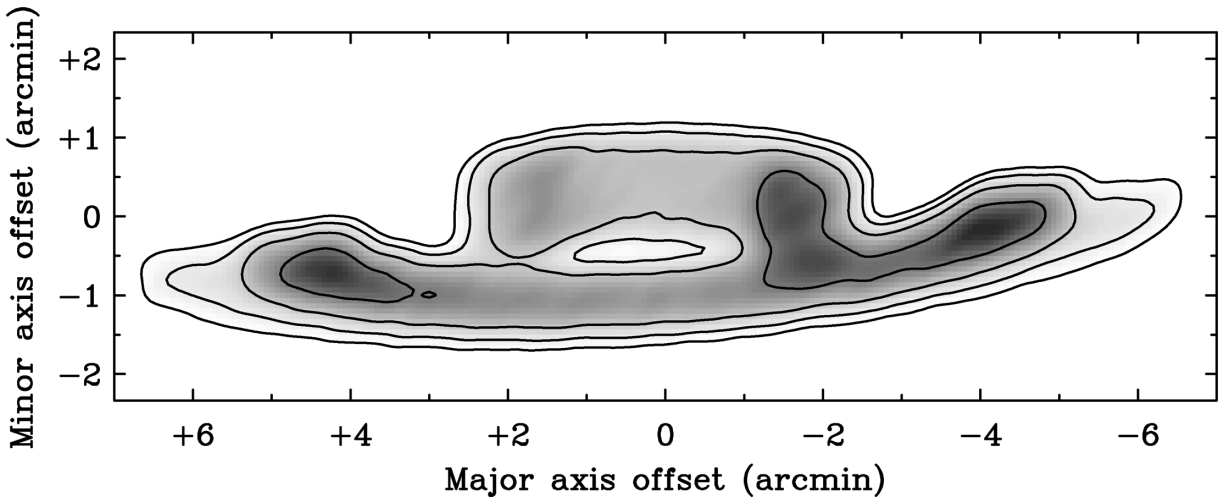

Figure 22. The column density of the arcs viewed edge-on. Contour levels are $2^n \times 1.3 \times 10^{19}$ cm^{-2}, $n = 0{-}3$.

enough to explain the individual features described in Section 2.2.1 (see Fig. 5). Unfortunately, the features are closely connected with the disc making it impossible to acquire reliable masses. Therefore, a simple comparison between the energy required to expel them from the disc and the SFR becomes impossible. However, Fig. 10 shows that the arms extend the longest in a single line of sight (the *x*-axis in Fig. 10) around 2 arcmin offset along the major axis (*y*-axis), very close to the locations of the features (Table 2). This and their proximity to the disc seem to point at an internal origin.

The difference between a lag obtained from a 'classical' model and the lag in our spiral arm model is driven by the presence of the arms in the line-of-sight warp. It is therefore questionable whether such asymmetries will have an effect in galaxies that, unlike NGC 5023, contain a significant thick disc or are perfectly edge-on with no pronounced asymmetries above the mid-plane. If the gas is pumped out of the plane by supernovae (SNe), it is logical to assume that the extra-planar gas close to the disc is densest above an area near the arms thus causing similar asymmetries above the plane. However, is there any observational evidence supporting such a picture? In the non-edge-on cases where anomalous gas has been detected the spiral arms cannot be identified in the anomalous component, either due to resolution problems or because a grand design spiral is absent. However, in the case of NGC 6946, the anomalous gas is clearly located towards the star-forming regions of the galaxy (Boomsma et al. 2008) and at the highest velocity offsets ($|\Delta v| \geq 80$ km s^{-1}, their fig. 9) a clear asymmetry in the distribution is visible. An asymmetry can also be tentatively seen in the anomalous gas distribution of NGC 4559 (Barbieri et al. 2005, fig. 6). However, the anomalous gas in NGC 2403 appears to form a smooth circular disc (Fraternali et al. 2002). In the case of NGC 891, the extra-planar Hα distribution is likely to be correlated with the spiral arms (Kamphuis et al. 2007b). Even though, the thick H I disc of this galaxy is so massive ($M_{\rm H\,I\ thick\ disc} = 0.3\ M_{\rm H\,I\ total}$; Oosterloo et al. 2007) that it is unlikely that all the neutral gas is located above the arms, a non-cylindrically symmetric overdensity could suffice to significantly lower the derived lag as the line of nodes becomes more and more devoid of gas.

Although spiral arms are well motivated, there are still many caveats with the best-fitting model of NGC 5023. The only reason for assuming a two-arm grand design spiral is that it is the simplest

spiral arm model, but that does not mean that any other model with non-cylindrically symmetric features, e.g. a four-arm model or a flocculent spiral, cannot fit the data. Also, in our spiral arm model for NGC 5023 TIRIFIC has organized the arms in such a way that the effect on the observed vertical gradient is maximized, i.e. the overdensity is as far from the line of nodes as possible (see Fig. 10), thus minimizing the gradient. On the other hand, there is no real need to organize the gas in spiral arms. All that is required in order to simulate the lag is that the distance between the line of nodes and the gas increases as a function of distance to the central plane – a likely situation, as only in the case where the gas above the plane is, up to its maximum vertical extent, on the line of nodes would there be no effect on the derived rotational velocities.

Our models also do not explore radial motions or variations in dispersion. Such variations are observed in other galaxies (Fraternali et al. 2002; Barbieri et al. 2005; Oosterloo et al. 2007). A variation in the dispersion seems unlikely as a comparison between the final model and the data does not show any major discrepancy which could relate to a variation in dispersion with height (see Figs 7 and 9). However, radial motions are often associated with spiral arms and could help to reproduce the boxiness of the central channel maps (Fig. 8, bottom-left/top-right panel). There are several reasons why radial motions are not included in the models, first of all they would present another set of free parameters. Due to the edge-on orientation of the galaxy the location of the motions would be ill constrained. As they would only help to fix some minimal discrepancies between the data and the final model in the central channels the improvement of such a model would be minimal at best. We could constrain the radial motions by merely allowing their presence in the spiral arms of the final model; however, this model already has a high number of free parameters. Additionally, as discussed at the start of the previous paragraph, it is merely an example of a realistic gas distribution and therefore it would be very speculative to constrain radial motions to the arms in the model.

If it turns out that many of the observed vertical gradients are overestimated in current tilted ring models, this could have a profound impact on the theory of disc–halo interactions. The velocity difference between ballistic models and observed lags (Fraternali & Binney 2008) could become less pronounced. However, in the case of NGC 5023 the vertical gradient is affected due to an overdensity in the line-of-sight warp. Do asymmetries in diffuse thick discs have the same pronounced effect on the vertical gradient? In how many nearly edge-on galaxies is the line-of-sight warp discarded due to the omission of non-cylindrically symmetric modelling? To answer these question the addition of spiral arms to the tilted ring models should be investigated for previous and forthcoming results.

5.2 UGC 2082 and arc features

We turn our attention to the origin of the two modelled arcs in UGC 2082. We first reiterate that, unlike for NGC 5023, models that attempted to fit these features with spiral arms were a poor match to the data, weakening the possible interpretation of the emission as disc–halo cycled gas above spiral arms in this case. We note that UGC 2082 has a similarly low global SFR to NGC 5023, but a disc of much larger radial extent, and therefore we may expect weaker disc–halo cycling.

The southern arc is at large radii and for this reason too is unlikely to represent disc–halo cycled gas. UGC 2082 is also a very isolated galaxy: it is not a member of any group optically identified by Giuricin et al. (2000), while the closest galaxy with detected H I in a recent search with the Arecibo telescope is at a projected distance of 279 kpc (Taber, Minchin & AGES 2011), scaled to our distance. Therefore, the arc is unlikely to be due to a tidal interaction. Even if the arc represented an asymmetric warp, these tend to occur in rich environments (García-Ruiz, Sancisi & Kuijken 2002), while the same authors find that lopsidedness is associated with nearby companions. Therefore, it seems that the arc is a candidate for an accretion event, although this conjecture is based only on the lack of a plausible alternative explanation.

Since the northern arc is above the inner disc, one may yet ask whether it could be a result of a disc–halo flow, despite the low-SF activity, and keeping in mind that the extent of the structure is much larger than one would expect from a single kpc-scale supershell creation event. Nevertheless, one can estimate the number of SNe required to lift such a mass of gas to a certain height above the disc under several assumptions.

First, the potential energy of a mass of gas at a height z above a disc, in the case of an isothermal sheet, is given by Howk & Savage (1997):

$$\Omega = 10^{52}\ \mathrm{erg} \left(\frac{M_{\mathrm{cloud}}}{10^5\ \mathrm{M}_\odot}\right) \left(\frac{z_0}{700\ \mathrm{pc}}\right)^2 \left(\frac{\rho_0}{0.185\ \mathrm{M}_\odot\ \mathrm{pc}^{-3}}\right) \times \ln[\cosh(z/z_0)],$$

where M is the mass of the gas and z is its height above the plane, z_0 is the mass scaleheight of the disc and ρ_0 is the mass density in the mid-plane below the feature. We assume that the disc potential is the only relevant contributor to the potential here. For the disc scaleheight, we can use the relation between stellar scaleheight and rotation speed found by van der Kruit & de Grijs (1999) to infer a value of about 300 pc. We assume this is a reasonable approximation for z_0. For the mass density, we begin with the value adopted by Howk & Savage (1997) for NGC 891. We then assume that the total stellar masses follow the stellar-mass Tully–Fisher relation of Kregel, van der Kruit & Freeman (2005), to find that the stellar mass of UGC 2082 should be 0.035 that of NGC 891. We next assume that a rough, average stellar density ratio of the two galaxies can be determined from this ratio by scaling by the product of the *K*-band disc area and scaleheight. The disc areas are taken from the 2MASS survey (Skrutskie, Cutri & Stiening 2006), while the scaleheights are assumed to follow the correlation with rotation speed from van der Kruit & de Grijs (1999). We thus estimate a mid-plane density of $0.04\,\mathrm{M}_\odot\,\mathrm{pc}^{-3}$ for UGC 2082. This is of course only a rough average for the whole disc. Using half of the vertical extent of the arc for z (1.4 kpc), we find a potential energy of about 1.0×10^{54} erg. Assuming 10^{51} erg per Type II SN, and if about 10 per cent of this energy goes into the kinetic energy of the gas (Mac Low & McCray 1988), then 10^4 SN are required. If the vertical velocity of the gas is $50\,\mathrm{km\,s}^{-1}$ [conservatively at the slow end of expansion velocities in the superbubble model of Mac Low, McCray & Norman (1989)], then the time-scale to lift the gas to this height is 3×10^7 yr, and the SN rate then required is $3 \times 10^{-4}\,\mathrm{yr}^{-1}$. Using the relation between the Type II SN rate and the SFR from Maoz et al. (2011), the total Type II SN rate in UGC 2082 is $4 \times 10^{-4}\,\mathrm{yr}^{-1}$. Thus, it seems, essentially all of the SNe at this rate would need to occur in this small part of the disc in order to raise this gas from the plane. Although the uncertainties are many, it does therefore appear unlikely that the arc can be explained as a result of disc–halo cycling. Therefore, an accretion origin cannot be ruled out.

We searched our HALOSTARS image for optical emission that might be associated with the arcs. A faint galaxy of detectable angular extent roughly 20 arcsec $\times$10 arcsec at RA $02^{\mathrm{h}}36^{\mathrm{m}}24.^{\mathrm{s}}6$, Dec. $25^\circ22'40.''4$ is coincident with the southern arc. However, this

may be a background galaxy. The Sloan Digital Sky Survey provides no additional information as it did not cover this area, while there is no coincident radio source in the NRAO VLA Sky Survey (Condon et al. 1998), or in *GALEX* NUV and FUV (1266 and 1574 s exposure times, respectively) images that we have obtained as part of the HALOGAS project.

6 SUMMARY AND CONCLUSIONS

We have investigated deep H I observations of the small galaxies UGC 2082 and NGC 5023. These observations were obtained as a part of the HALOGAS Survey and will contribute to our understanding of disc–halo interactions and cold gas accretion in the local Universe. We have constructed detailed tilted ring models of these galaxies and compared these to the full 3D information available in the observed H I cubes. Through a new functionality in TIRIFIC that allows the addition of localized overdensities to the models, we have, for the first time, investigated the effect of non-cylindrically symmetric distributions of the neutral hydrogen on the observed data.

In the case of NGC 5023, a 'classical' analysis, without non-cylindrically symmetric components, would lead us to conclude that this galaxy has no line-of-sight warp nor a flare but merely a single disc with a scaleheight of 10.5 arcsec (0.34 kpc) with a radially varying lag. This lag would be $\sim -14.9\,\mathrm{km\,s^{-1}\,kpc^{-1}}$ in the centre of the galaxy and drop to $0\,\mathrm{km\,s^{-1}\,kpc^{-1}}$ between 133 arcsec (4.3 kpc) and 304 arcsec (9.7 kpc) radial offset. As usual for this kind of modelling, the two sides of the disc were treated independently. However, if we include non-cylindrically symmetric distributions, the fit to the data is significantly improved provided that the disc is warped in the line of sight. Compared to the 'classical' analysis the scaleheight of the main disc is somewhat lower (9 arcsec, 0.29 kpc), the derived lag is significantly lowered and radial variation of the lag no longer improves the fit to the data. Additionally, the underlying main disc is now almost fully cylindrically symmetric and all the asymmetry is in the warp and the localized overdensities.

No lag is required for UGC 2082, but two arcs (features of limited extent in azimuthal angle in the disc) with a large vertical extent and masses of the order of 10^8 $M_\odot$ each are necessary to reproduce prominent asymmetries in the gas distribution and kinematics. The main disc to which they are added still requires a warp. One arc is at relatively large radii and features a slightly different inclination and PA to the main disc, while the other is found above the inner disc. Given the lack of nearby companions, and the insufficient SFR that could be responsible for these features, they may be examples of ongoing accretion.

ACKNOWLEDGEMENTS

PK would like to thank the German Humboldt Foundation for the financial support during his stay in Germany. RJR, RAMW and MTP acknowledge support from the National Science Foundation under grant AST-0908126 to RJR and RAMW. GG is a postdoctoral researcher of the FWO - Vlaanderen (Belgium). PS is an NWO/Veni fellow. The work of WJGdB was supported by the European Commission (grant FP7-PEOPLE-2012-CIG #333939). This publication makes use of data products from the Two Micron All Sky Survey, which is a joint project of the University of Massachusetts and the Infrared Processing and Analysis Center/California Institute of Technology, funded by the National Aeronautics and Space Administration and the National Science Foundation. The Westerbork Synthesis Radio Telescope is operated by ASTRON (the Netherlands Institute for Radio Astronomy) with support from the Netherlands Foundation for Scientific Research (NWO). The authors also want to extend their thanks to the other members of the HALOGAS collaboration who have contributed with useful discussions on the paper. Finally, we would like to thank the referee for carefully reading the manuscript and providing useful comments.

REFERENCES

Barbieri C. V., Fraternali F., Oosterloo T., Bertin G., Boomsma R., Sancisi R., 2005, A&A, 439, 947
Barnabè M., Ciotti L., Fraternali F., Sancisi R., 2006, A&A, 446, 61
Benjamin R. A., 2002, in Taylor A. R., Landecker T. L., Willis A. G., eds, ASP Conf. Ser. Vol. 276, Seeing Through the Dust: The Detection of HI and the Exploration of the ISM in Galaxies. Astron. Soc. Pac., San Francisco, p. 201
Boomsma R., Oosterloo T. A., Fraternali F., van der Hulst J. M., Sancisi R., 2005, in Braun R., ed., ASP Conf. Ser. Vol. 331, Extra-Planar Gas. Astron. Soc. Pac., San Francisco, p. 247
Boomsma R., Oosterloo T. A., Fraternali F., van der Hulst J. M., Sancisi R., 2008, A&A, 490, 555
Bothwell M. S. et al., 2011, MNRAS, 415, 1815
Bregman J. N., 1980, ApJ, 236, 577
Byrd G. G., 1978, ApJ, 222, 815
Collins J. A., Benjamin R. A., Rand R. J., 2002, ApJ, 578, 98
Condon J. J., Cotton W. D., Greisen E. W., Yin Q. F., Perley R. A., Taylor G. B., Broderick J. J., 1998, AJ, 115, 1693
Dalcanton J. J., Yoachim P., Bernstein R. A., 2004, ApJ, 608, 189
de Vaucouleurs G., de Vaucouleurs A., Corwin H. G., Jr, Buta R. J., Paturel G., Fouque P., 1992, VizieR Online Data Catalog, 7137, 0
Fraternali F., Binney J. J., 2008, MNRAS, 386, 935
Fraternali F., van Moorsel G., Sancisi R., Oosterloo T., 2002, AJ, 123, 3124
Fraternali F., Oosterloo T. A., Sancisi R., Swaters R., 2005, in Braun R., ed., ASP Conf. Ser. Vol. 331, Extra-Planar Gas. Astron. Soc. Pac., San Francisco, p. 239
García-Ruiz I., Sancisi R., Kuijken K., 2002, A&A, 394, 769
Gentile G. et al., 2013, A&A, 554, A125
Giuricin G., Marinoni C., Ceriani L., Pisani A., 2000, ApJ, 543, 178
Heald G. H., Rand R. J., Benjamin R. A., Bershady M. A., 2006, ApJ, 647, 1018
Heald G. H., Rand R. J., Benjamin R. A., Bershady M. A., 2007, ApJ, 663, 933
Heald G. et al., 2011, A&A, 526, A118
Heald G. et al., 2012, A&A, 544, C1
Hoeft M., Gottlöber S., 2010, Adv. Astron., 2010, 693968
Howk J. C., Savage B. D., 1997, AJ, 114, 2463
Józsa G. I. G., Kenn F., Klein U., Oosterloo T. A., 2007, A&A, 468, 731
Kamphuis P., Peletier R. F., Dettmar R.-J., van der Hulst J. M., van der Kruit P. C., Allen R. J., 2007a, A&A, 468, 951
Kamphuis P., Holwerda B. W., Allen R. J., Peletier R. F., van der Kruit P. C., 2007b, A&A, 471, L1
Kamphuis P., Peletier R. F., van der Kruit P. C., Heald G. H., 2011, MNRAS, 414, 3444
Kaufmann T., Mayer L., Wadsley J., Stadel J., Moore B., 2006, MNRAS, 370, 1612
Kennicutt R. C., Jr, 1981, AJ, 86, 1847
Kennicutt R. C., Jr, Tamblyn P., Congdon C. E., 1994, ApJ, 435, 22
Kereš D., Katz N., Weinberg D. H., Davé R., 2005, MNRAS, 363, 2
Kregel M., van der Kruit P. C., Freeman K. C., 2005, MNRAS, 358, 503
Lee S.-W., Irwin J. A., Dettmar R.-J., Cunningham C. T., Golla G., Wang Q. D., 2001, A&A, 377, 759
Mac Low M.-M., McCray R., 1988, ApJ, 324, 776
Mac Low M.-M., McCray R., Norman M. L., 1989, ApJ, 337, 141

Maoz D., Mannucci F., Li W., Filippenko A. V., Della Valle M., Panagia N., 2011, MNRAS, 412, 1508
Marinacci F., Fraternali F., Nipoti C., Binney J., Ciotti L., Londrillo P., 2011, MNRAS, 415, 1534
Matthews L. D., Wood K., 2003, ApJ, 593, 721
Muller C. A., Oort J. H., Raimond E., 1963, C. R. Acad. Sci. Paris, 257, 1661
Norman C. A., Ikeuchi S., 1989, ApJ, 345, 372
Oosterloo T., Fraternali F., Sancisi R., 2007, AJ, 134, 1019
Rand R. J., 1996, ApJ, 462, 712
Rossa J., Dettmar R.-J., 2003, A&A, 406, 505
Sancisi R., Allen R. J., 1979, A&A, 74, 73
Sancisi R., Fraternali F., Oosterloo T., van der Hulst T., 2008, A&AR, 15, 189
Schaap W. E., Sancisi R., Swaters R. A., 2000, A&A, 356, L49
Shapiro P. R., Field G. B., 1976, ApJ, 205, 762
Skrutskie M. F. et al., 2006, AJ, 131, 1163
Springob C. M., Haynes M. P., Giovanelli R., Kent B. R., 2005, ApJS, 160, 149
Swaters R. A., Sancisi R., van der Hulst J. M., 1997, ApJ, 491, 140
Taber T. M., Minchin R., , 2011, BAAS, 43, 246.06
van der Hulst J. M., Terlouw J. P., Begeman K. G., Zwitser W., Roelfsema P. R., 1992, in Worrall D. M., Biemesderfer C., Barnes J., eds, ASP Conf. Ser. Vol. 25, Astronomical Data Analysis Software and Systems I. Astron. Soc. Pac., San Francisco, p. 131
van der Kruit P. C., de Grijs R., 1999, A&A, 352, 129
van der Kruit P. C., Freeman K. C., 2011, ARA&A, 49, 301
van Woerden H., Wakker B. P., 2004, in van Woerden H., Wakker B. P., Schwarz U. J., de Boer K. S., eds, Astrophysics and Space Science Library, Vol. 312, High Velocity Clouds. Kluwer, Dordrecht, p. 195
Wakker B. P., van Woerden H., 1997, ARA&A, 35, 217
Westmeier T., Braun R., Thilker D., 2005, A&A, 436, 101
Zschaechner L. K., Rand R. J., Heald G. H., Gentile G., Kamphuis P., 2011, ApJ, 740, 35
Zschaechner L. K., Rand R. J., Heald G. H., Gentile G., Józsa G., 2012, ApJ, 760, 37

This paper has been typeset from a TEX/LATEX file prepared by the author.